

Effect of thin layer thickness of iron oxide prepared by sol-gel on the opto-electronic properties of the material

M. S. Ferah^a, A. Bazine^a and S. Sedira^b

^aLaboratoire de physique chimie des semi-conducteurs (LPCS), département de physique, université Constantine 1

^bLaboratoire de céramiques, département de physique, université Constantine 1

Received date: May 25, 2014; revised date: December 10, 2014; accepted date: December 21, 2014

Abstract

Thin Hematite iron oxide layers (α Fe₂O₃) were synthesized successfully using FeCl₃ as precursor, ethanol as solvent and acetic acid as catalyst according to the sol-gel process and spin-coating technique. The structural properties of the films were investigated by X-ray diffraction (XRD), scanning electron microscopy (SEM) and Raman spectroscopy, and optical properties by the UV-Vis spectroscopy. This study shows a singular behavior of optical transmission characterized by two bearings and a clear dependence of optoelectronic parameters with film thickness.

Keywords: Sol-Gel, iron oxide, nanomaterials, transmittance, optical constants, optical gap.

1. Introduction

The Biological or chemical water pollution has been an alarming increase in the last 50 years due to the intensification and diversification of industries. For wastewater treatment, heterogeneous photocatalysis is a process booming [1]. The materials suitable for this operation are micro and nanostructured wide bandgap semiconductors. They are oxides or sulphides of noble metals, or, more often, for reasons of cost and stability, oxides or sulphides of transition metals [1]. Among these materials, iron oxide Fe₂O₃ is a very good n type photocatalyst [2]. Its 2.1 eV gap allows a sensitivity in the visible range from 0.6 microns. With a very low price, an excellent stability and a non-toxicity under ambient conditions, Fe₂O₃ is widely used in photocatalysis, gas detection, photoelectrodes, magnetic devices and lithium batteries [3]. The sol-gel process is a chemical way very easy to implement [4], it boils down to put and properly spread a solution containing the concerned metal ion, calcining the deposit in order to remove organic compounds present in then the solution, annealing the layer to ambient air in order to ensure oxidation of the metal and crystallization of the material.

2. Experimental

2.1. Préparation of the solution

The chemicals used in preparing solutions are iron chloride hexahydrate (FeCl₃ · 6 H₂O) 97% Aldrich as precursor, ethanol (C₂H₅OH) Aldrich 96% as solvent and acetic acid (CH₃COOH) Aldrich 99% as catalyst. The solution was prepared and synthesized at room temperature as follows: a definite quantity of each of the three products were measured in the molar proportions FeCl₃-ethanol-acetic acid-water : 1-225-9.5-30. The solvent is then poured into the vessel containing the solid precursor while stirring with a magnetic stirrer during half an hour. Finally the catalyst is drip added and the solution is stirred for one hour. The solution is then ready for use.

2.2. Layer déposition

The substrates used are analysis glass slides (2x1 cm) previously cut and cleaned in ultrasonic baths of acetone, methanol and distilled water for 15 minutes each time. Once dried, the substrate is fixed on the rotating part of the spin coater and then the layers are deposited at a rate of three drops for each sublayer. The rotation speed is 500 rev/min and the time 20s. Each sublayer is followed by drying at 100 °C for 10

min in a muffle furnace and, finally, the layer is annealed at 500 °C in the same oven for 1 hour. We fabricated four layers each having a different number of sublayers (table 1).

Layer	Nb sublayers
6F1	1
6F2	2
6F3	3
6F5	4

Table 1 : Number of sublayers in each sample.

2.3. Analysis techniques

The morphology of the layers was analyzed by scanning electron microscopy (SEM) on a device of the type "JEOL JSM 7001F FEG SEM" with an acceleration voltage of 5-15 kV. The crystal structure was characterized by X-ray diffraction (XRD) on the diffractometer "D8 Advance AXS Brunker" in shaving mode with monochromatic radiation $\text{CuK}\alpha_1$ ($\lambda = 1,54056 \text{ \AA}$). The characterization of the phases was made by Raman spectroscopy with the spectrometer "Bruker SENTERRA" in the range 0 to 4000 cm^{-1} . Finally, thickness and optical properties of the layers were evaluated by study of the transmission spectra in the wavelength range of UV-Visible (200-800 nm), with a double beam spectrophotometer "JASCO V670

3. Résultats and discussion

3.1. Morphology

Figure 1 shows the microstructure of the surface layers Fe_2O_3 .

At low magnification (x 1000), the micrograph (1a) shows an inhomogeneous deposition covering some areas and leaving others completely naked. At high magnification (x 8000) micrograph (1b) shows a structure of grain sizes of up to 200 nm.

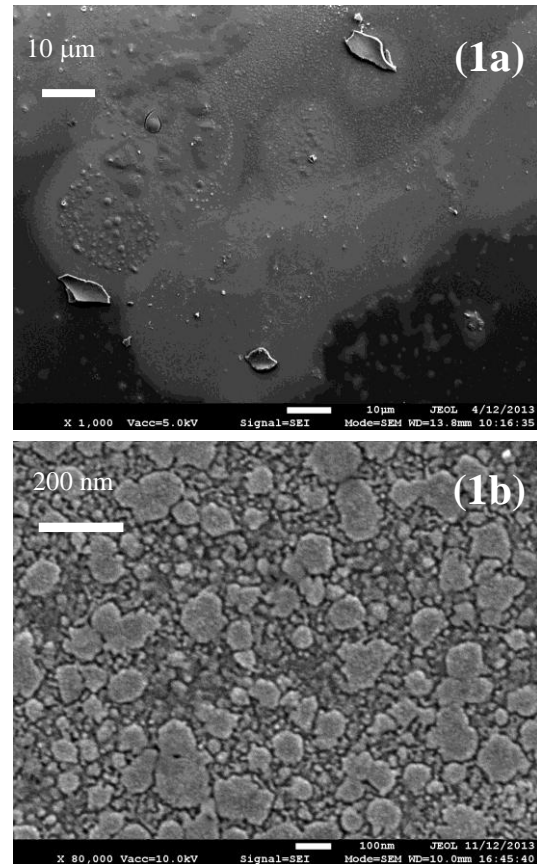


Figure 1 : SEM micrographs of Fe_2O_3 layers.

3.2. Structural properties

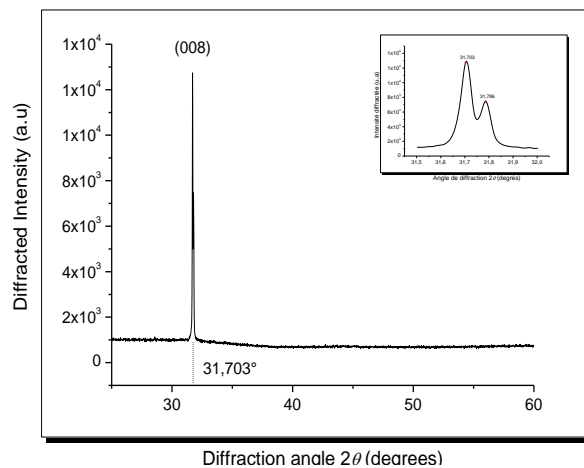


Figure 2 : XRD diffraction spectrum layers

XRD measurements of the four layers provide substantially the same record (figure 2). It consists of a single peak at $2\theta = 31.703^\circ$. The nearest peak on

the ASTM specifications is located at $2\theta=31.719^\circ$ and corresponds to (008) plane of Hematite phase ($\alpha\text{-Fe}_2\text{O}_3$). We therefore conclude that our material is mainly the Hematite phase ($\alpha\text{-Fe}_2\text{O}_3$) of iron oxide. As for the exclusive presence of a single peak, this would mean a preferential growth along the axis perpendicular to this plane [5].

The development of this peak revealed a doublet : 31.703° and 31.786° . Assuming the two peaks from the same plane, the application of the Bragg law $n\lambda=2d\sin\theta$ gives for the second peak : $\lambda'=1.5445 \text{ \AA}$ corresponding to $\text{CuK}\alpha_2$ line of X-ray generator.

In addition, the spectrum also allows us to estimate the average grain size D from the empirical Scherrer law [5] :

$$D = \frac{0,9\lambda}{\Delta\theta.\cos\theta} \quad (1)$$

Where λ and θ are respectively the wavelength and the diffraction angle of the largest peak and $\Delta\theta$ the half-height width of this peak. The evaluation of these quantities on the diffraction pattern of Figure 2 gives : $D=170 \text{ nm}$.

3.3. Raman Spectroscopy

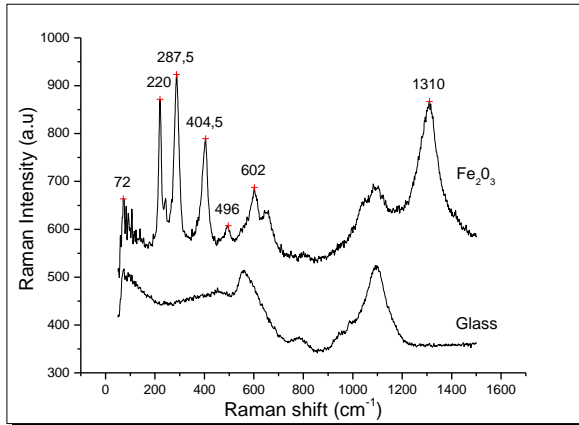


Figure 3 : Raman spectra of Fe_2O_3 layers

Figure 3 shows the typical Raman spectrum of Fe_2O_3 layers. The peaks 220; 287.5; 404.5; 496 and 1310 cm^{-1} belongs to Hematite phase [8] but are offset

5 to 7 cm^{-1} because the variation of the crystallinity and the grain size, as explains Alian et al. [6].

3.4. UV-Visible spectroscopy

In figure 4 are shown the four optical transmission spectra of Fe_2O_3 layers. These spectra show a singular appearance composed of three common areas of high absorption in the UV range of 200-300 nm, low absorption in the visible range of 600-800 nm and average absorption between the two areas with a remarkable level of low absorption between 300 and 400 nm.

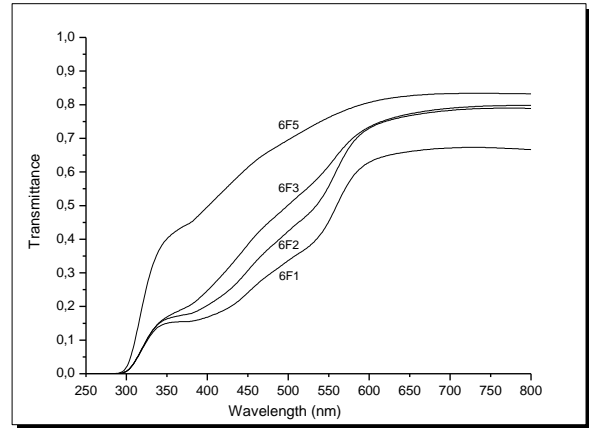


Figure 4 : Transmittance of Fe_2O_3 layers.

The transmittance of thin films obeys to the law [7]:

$$T = \frac{Ax}{B + Cx + Dx^2} \quad (2)$$

where : $A = 16s(n^2 + k^2)$

$$B = [(n+1)^2 + k^2][(n+s)^2 + k^2]$$

$$C = 2[-(n^2 - 1 + k^2)(n^2 - s^2 + k^2) + 4k^2s].\cos\varphi - 4k[s(n^2 - 1 + k^2) + (n^2 - s^2 + k^2)].\sin\varphi$$

$$D = [(n-1)^2 + k^2][(n-s)^2 + k^2]$$

$$\varphi = 4\pi d/\lambda ; x = \exp(-\alpha d)$$

k : Extinction index layer.

n : Refractive index layer.

s : Refractive index substrate ($s=1.52$).

λ : Wavelength.

d : Layer thickness.

The fit of this relationship was used to estimate the layer thicknesses and optical constants. Figure 5 shows the thicknesses depending on the number of sublayers deposited with an average of 374.5 nm in a sublayer.

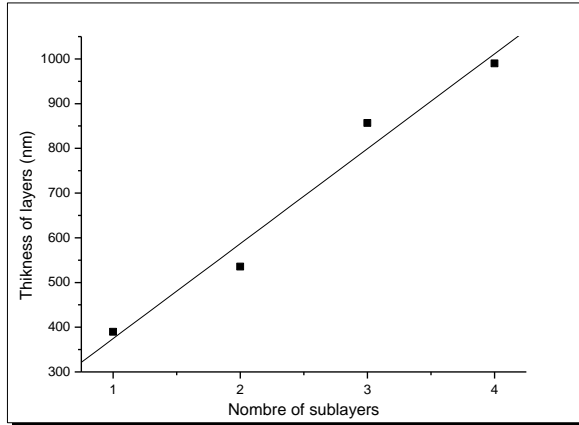


Figure 5 : Thickness of Fe_2O_3 layers.

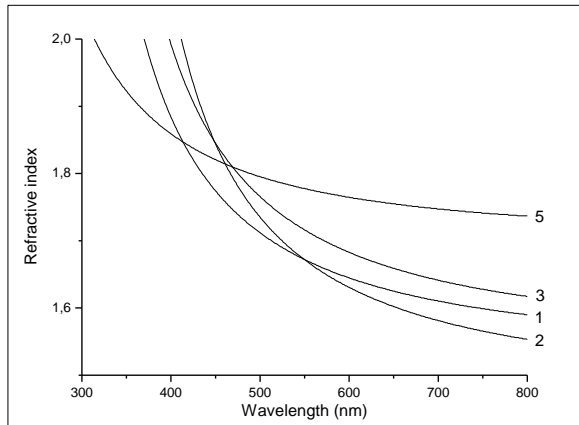


Figure 6 : Refractive index of Fe_2O_3 layers.

Figure 6 shows the variation of the refractive index as a function of wavelength. This variation shows a common appearance with very high values in the UV region of strong absorption decreases greatly in the visible range of approaching the value of 1.74 for the thickest layer.

Figure 7 shows the variation of the extinction index as a function of the wavelength. This quantity

decreases rapidly from a high value in the UV to near-constant value of 0.03 in the visible.

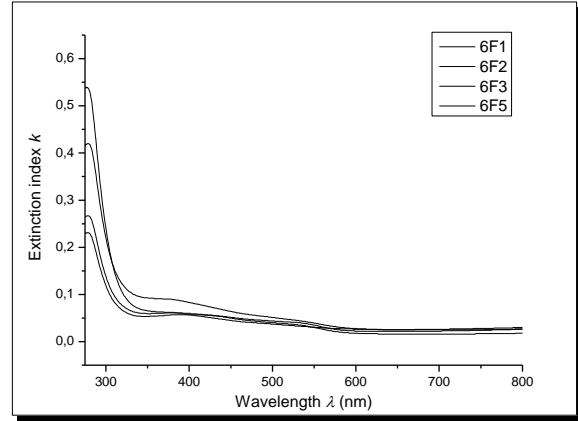


Figure 7 : Extinction index of Fe_2O_3 layers.

From this quantity we estimated the absorption coefficient α in accordance with the relationship law [7]:

$$\alpha = \frac{4\pi k}{\lambda} \quad (3)$$

where λ is the wavelength of the incident photons.

In the region of strong absorption, this coefficient is connected to the energy of the incident photons by the Tauc relation [8] :

$$(\alpha h\nu)^m = K(h\nu - E_g) \quad (4)$$

where E_g is the optical gap, K a constant independent of energy, and m a constant describing the transition mode gap, direct ($m = 2$) or indirect ($m = 1/2$). In practice, this law is linear over a large area of the region of strong absorption and becomes curve to approach the optimal absorption. The gap is deduced by extrapolating the linear portion to the point $\alpha = 0$.

In our case, the indirect mode seems more probable because of the gap values deduced. Indeed, in the region of low energies we meet the energy gap of the different layers (Figure 8) and note significant differences ranging from 1.19 eV for the 6F1 layer (390 nm) to 1.76 eV for the 6F3 layer (850 nm).

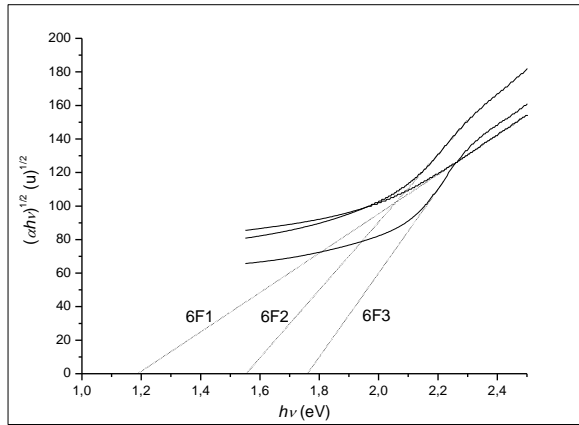


Figure 8 : Curves $(\alpha hv)^{1/2} = f(hv)$ at low energies.

These values are below the usual value 2.1 eV for Fe_2O_3 but tend to this value for larger thicknesses (Figure 9) according to an empirical exponential law of the form :

$$E_g = 2,054[1 - \exp(-0,0024x)] \quad (5)$$

where x is the layer thickness.

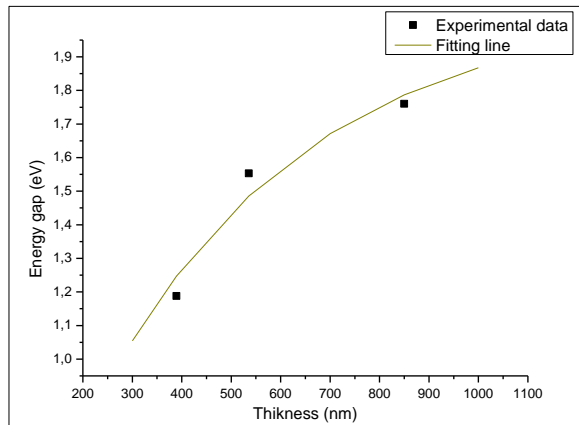


Figure 9 : Energie gap according to layer thickness.

4 . Conclusion

Thin films of Fe_2O_3 were deposited on glass substrates by the sol-gel process and spin-coating technique. SEM micrographs show a nanosized granular structure of around 170 nm. XRD spectra consist of a single peak of (008) plane of Hematite phase ($\alpha\text{-Fe}_2\text{O}_3$), indicating a preferential growth

perpendicular to this plane. Raman spectroscopy confirms the sole presence of Hematite phase with peaks shifted due to the nanocrystalline structure. The thickness of the layers is in accordance with the number of sublayers deposited. The optical constants n and k vary slightly depending on the thickness near normal values $n=1.74$ and $k=0.03$. However, the gap shows a large dependence on the layer thickness with a tendency to the usual value 2.1 eV for thick layers.

References :

- [1] Saber Ahmed, M.G. Rasul, Wayde N. Martens, R. Brown, M.A. Hashib, Desalination 261 (2010) 3-18.
- [2] Young Ug Ahn, Eui Jung Kimb, Hwan Tae Kimc, Sung Hong Hahn, Materials Letters 57 (2003) 4660-4666
- [3] Jacques Livage, Revue Verre, Vol 6, No 5. (2000).
- [4] R. Mechiakh, N. Ben Sedrine, J. Ben Naceur, R. Chtourou, Surface & Coatings Technology 206 (2011) 243-249.
- [5] K.F. Konan, B. Hartü, B. Aka, A. Ridah, K. Dakhsi, Y. Arba et P. Thevenin, Afrique Science 06 (1) (2010) 29-37
- [6] Alian Wang, L. A. Haskin, and B. L. Jolliff, Dept. Earth & Planetary Sciences and the McDonnell Center for Space Sciences, Washington University, St. Louis, MO 63130. (alianw@levee.wustl.edu).
- [7] J.C. Manificier, J. Gasiot and J.P. Fillard, Journal of Physics E: Scientific Instruments 1976 Volume 9, 1002-1004
- [8] L. Dghoughi, B. Elidrissi, C. Bernede, M. Addou, M. Alaoui Lamrani, M. Regragui, H. Erguig, Applied Surface Science 253 (2006) 1823-1829.

Thanks :

SEM measurements were made graciously by Gaëlle Amiri at GEMaC of St Quentin University of Versailles in France.

Modelisation of photocourant in organic solar cell using Phthalocyanine/Perylene

S. Bouchekouf, A. Marir, A. Merzougui and F. kbailli

Département d'électronique, Faculté des sciences de l'ingénieur, Université Mentouri, Constantine, Route d'Ain El Bey,
25000 Constantine, Algérie. E-mail : bouchekoufs@yahoo.fr

Received date: May 25, 2014; revised date: December 13, 2014; accepted date: December 21, 2014

Abstract

In this paper, we report on investigation uses a method of calculation the photocurrent delivered by the organic solar cell double-layer MPP/ZnPc applying the equations of continuities and the currents by analogy to the phenomena of loads transport according to the model of an heterojunction n/p. The principal generation of the photocurrent is localized in the active zone, a very fine area by contribution with the thicknesses of the donor and acceptor layers. Thus let us that the excitons dissociate only in the MPP/ZnPc interface, whereas the zone of absorption is considerably larger than the diffusion length.

The principal photovoltaic parameters of this structure are calculated by the simulation of equation $I(V)$, under illumination $AM_{1.5}$. Insertion of the composite layer C60 and ZnPc in the interface of MPP and ZnPc makes it possible to improve the performances of the cell by an increase in the photocurrent of the value 2.6 mA/cm^2 to 5.3 mA/cm^2 and the conversion efficiency η from 0,72% to 1,49%.

We worked out a numerical model based on resolution of equations of continuities who gave results in good accordance with literature and which allowed, moreover a better control of performances of organic cells, for their improvement.

Key words: organic solar cell; MPP/ZnPc structure; photocurrent; equation of continuity.

1. Nomenclature

$D_n = \frac{\mu_n KT}{q}$ Diffusion constant of electrons.

$D_p = \frac{\mu_p KT}{q}$ Diffusion constant of holes.

μ_n Mobility of electrons.

μ_p Mobility of holes.

$\Delta n = n - n_e$ Density of excitons generated (electrons), n_e : density in balance.

τ_n Life time of minority carriers of area p (electrons).

$\Delta p = p - p_e$ Density of generated holes, p_e : density in balance.

τ_p Lifespan of minority carriers of area n (holes).

G_n Rate of electrons generation.

G_p Rate of holes generation.

$\Phi(\lambda)$ Flux of incidents photons by cm^2 by s^{-1} by unit of wavelength.

R , Reflexion coefficient.

α_i , Absorption coefficient in MPP.

x_i , Thickness of the ZnPc layer.

L_p Diffusion length of holes.

S_p , Speed of recombination of the holes on the surface.

α_2 , Absorption coefficient in ZnPc.

S_n , Speed of recombination of the electrons to the back contact.

L_n Diffusion length of the electrons

I , Current

I_{cc} , Short-circuit current

J , Current density

V , Tension

V_{oc} , Open circuit tension.

FF, Fill factor.

η , Conversion efficiency.

2. Introduction

Molecular electronics is a quickly developing field and the organic conducting materials were employed like active medium in the optoelectronic devices such as the luminescent diodes (LED), the field-effect transistors, sensors, lasers, the photodiodes and the solar cells. The organic solar cells drew a significant attention, because of their characteristic to be implemented by the promise of inexpensive manufacture and the large variety of functionality of organic materials [1, 2].

The performances of a solar cell depend on the thin layers between the electrodes. During two last decades, two types of organic solar cells were intensively studied: those built with a stacking of two organic layers (double-layer) and the others which use a built composite layer of a homogeneous mixture of two materials of the cell.

We propose in this investigation, contrary to the literature where the results are only experimental, a method of simulation based on the resolution of the equations of currents (continuities) for an organic solar heterostructure containing pigment methyl perylene (MPP) and the phthalocyanine of zinc (ZnPc) with like ITO/MPP/ZnPc/Au structure. These organic dyes have a good thermal stability, high absorption coefficients ($> 10^5 \text{cm}^{-1}$), and a sufficient electric conductivity, although the thickness of the useful layer of generation the carriers in organic cells is much finer than that of inorganic cells, the appreciable power conversion efficiency can be reached because of the high absorption coefficients. As p-conducting (ZnPc) and n-conducting (MPP) materials.

2. Description and mechanisms of generation in the organic cells

The currently allowed photovoltaic process is the absorption of a photon by the active organic layer which generates an exciton (instead of the free carriers in the inorganic case) which diffuses through the material [3]. If the diffusion length of the exciton is sufficiently large to meet an internal field, the separation of the loads can take place. Hole and electron are then collected with the electrodes (respectively with the anode and cathode) according to the internal field of the cell. We go in what follows to describe the various architectures met in the organic cells photovoltaic and their own mechanisms.

2.1. The single-layer structure (Schottky)

The organic photovoltaic cells described as being of Schottky type with a conversion efficiency of 0,7% under AM_1 illumination, are presented in the form metal/organic/metal or ITO/organic/metal [4]. In this kind of structures, the properties of the cell are strongly related to the electrodes; moreover this structure presents a weak fill factor FF [5]. In order to increase the total conversion efficiency of a mono layer photovoltaic cell, a photovoltaic diode based on a Schottky structure was carried out with pentacene doped (iode or brome). The double-layer structure thus proves necessary for the improvement of the performances.

2.2. The double-layer structure (Heterojunction)

The structure of a double-layer cell is represented on (Fig. 1). To obtain an heterojunction of the type PN, the electrodes are selected so that one obtains ohmic contacts with organic films. The ITO is often used as semi-transparent electrode because, on the one hand it presents a transmittance of more than 85% in the visible one and on the other hand it presents an ohmic contact with certain conveying materials of holes (MPc, PTCDA...) [6]. The back electrode consists of metals like Al, Ag or of Mg:Ag alloy which make it possible to obtain an ohmic contact with materials of the type n [7].

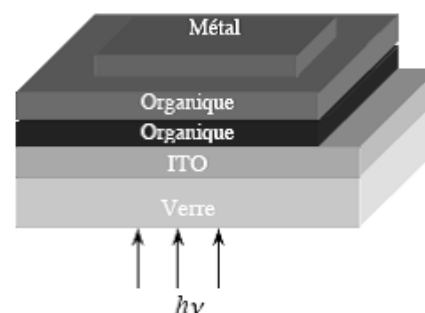


Fig. 1: Configuration of the structure of a double-layer photovoltaic cell [9].

2.2.1. Physical principles of organic solar cell

In the structures with heterojunction, the design and the collection of the photoinduced charges follow the following process, where the materials donor and acceptor develop an interface able to separate the carriers [8].

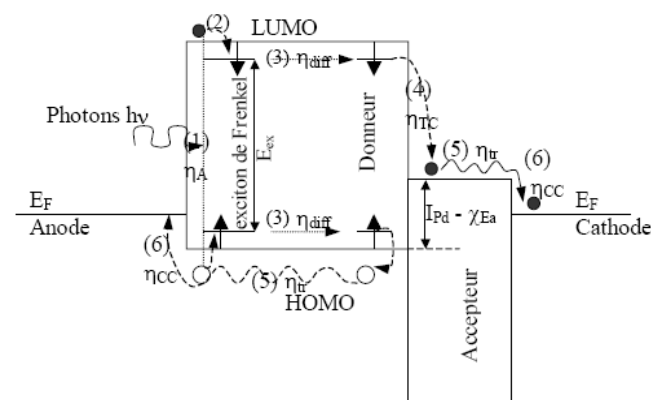


Fig. 2: mechanisms of the generation of carriers in an organic heterojunction [10].

(1) Photonic absorption.

(2) Generation of excitons

(3) **Diffusion of the exciton:** The exciton diffuses towards the interface between organic materials. If excitons are generated at a distance lower than L_{exc} (called diffusion length of excitons), they can diffuse until the interface, so not they recombine.

(4) **Separation of the carriers:** The dissociation of the exciton is done with the interface between two materials. If the life-time of the excitation is sufficient so that the exciton meets an internal field, it appears a separation of the hole and electron.

(5) Transport of the carriers towards the electrodes

(6) Collect carriers with the electrodes.

2.2.2. Double-layer structures containing small molecules

More recent studies of a cell manufactured starting from perylene (MPP) and phthalocyanine (ZnPc) with as structure Au/MPP/ZnPc/Al [11] show that the generation of carriers appears only on the level of a very fine area of the active layer. The insertion of a layer made up of a mixture of C_{60} and ZnPc (1:1) between ZnPc and MPP

makes it possible to reach a conversion efficiency of 1, 05 % under $AM_{1.5}$ [12].

2.2.3. Heterojunction containing polymer and C60

The first polymer organic solar cell is an architecture combining C_{60} and one polymer like the PPP (polyparaphenylene) [13], the PPV (para phenylènevinylene) [14]. C_{60} (Buckminsterfullerene) being a molecular organic compound comparable to an intrinsic semiconductor with gap direct [15, 16]. These cells present very weak conversion efficiency.

2.2.4. Heterojunction with only polymers

In the structures in interpenetrated networks the composite layer is a mixture of two polymers elements donors/acceptors, this technology improves the performances of the double-layer organic solar cells.

- Example of materials used:
 - Donor: the P3HT (poly (3-hexylthiophene), MEH-PPV (poly (2-methoxy-5(2'-ethyl-hexyloxy)-p-phenylenevinylene) [17], MDMO-PPV (poly (2-methoxy-5-dodecyloxy-p-phenylene vinylene) [18].
 - Acceptor: C_{60} , [6-6]-phenyl C_{60} butyric acid methyl ester (PCBM), C_{60} [19].
- Conversion efficiencies reached [20-22]:
 - 3,3% composite : MDMO-PPV/ PCBM (2002).
 - 5% composite : P3HT/PCBM (2005/2006).

3. Simulation of the double-layer organic cell MPP/ZnPc

In our study we interest in a doublelayer-structure containing small molecules described in paragraph 2.2.2.

The MPP/ZnPc heterojunction of the organic cell ITO/MPP/ZnPc/Au presented on (fig. 3), is a structure donor/acceptor. It allows the effective transfer of the photoelectrons since ZnPc which plays the role of donor towards the acceptor MPP. The two electrodes are made up of ITO and Au. The ITO often presents a semi-transparent electrode. The back electrode consists of Au. A layer made up of a mixture of C_{60} and ZnPc (1:1), is inserted between the MPP and ZnPc to increase the number of dissociation cites of excitons. The cell that we studied is consisted of the structure: substrat/ITO (30nm)/MPP (20nm)/ZnPc (220)/Au (40nm) [23].

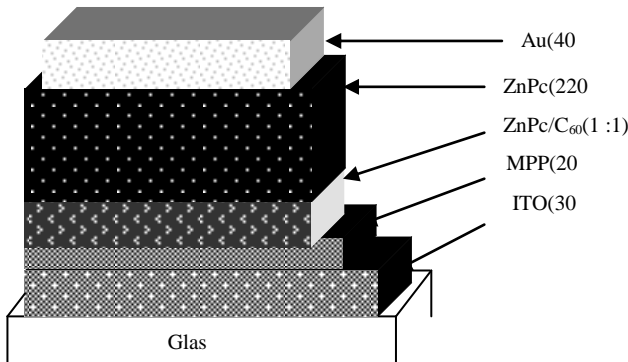


Fig. 3: Structure of the substrat/ITO/MPP/ZnPc/Au cell [23].

3.1 Calculation of MPP/ZnPc cell current

The absorption for the double-layer structure represented on (fig. 3) is carried out in the two layers. In this configuration only the excitons generated in the vicinity of the interface are effective for the generation of the photocurrent, this photocurrent is the sum of the current generated on the level of donor and the current in the acceptor.

For the simulation of the photocurrent of the cell one uses the geometry of (Fig. 4).

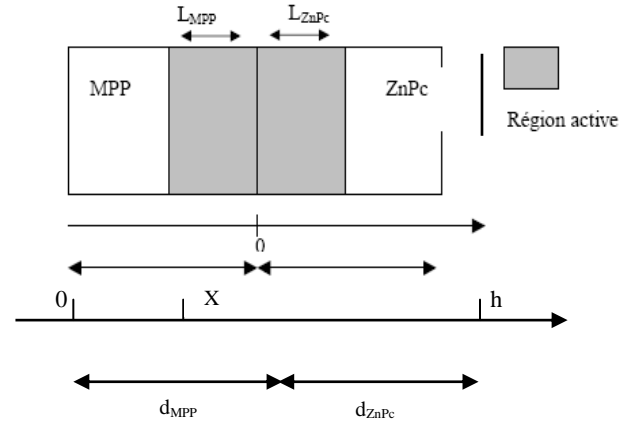


Fig. 4 : Geometrical model of the MPP/ZnPc structure [23].

Where D_{MPP} , D_{ZnPc} are dimensions of layers MPP and ZnPc respectively and L_{MPP} , L_{ZnPc} , diffusion lengths. For calculation takes some $L_{MPP}=1$ nm and $L_{ZnPc}=5$ nm.

The numerical resolution of the equations of continuities and the currents, by the iterative method allowed to determine the distribution of excitons along the cell and to deduce the equation which characterizes the current for each point of the cell.

$$\frac{\partial n}{\partial t} = G_n - \frac{\Delta n}{\tau_n} + \frac{1}{q} \text{div}(J_n) \quad (1)$$

$$\frac{\partial p}{\partial t} = G_p - \frac{\Delta p}{\tau_p} - \frac{1}{q} \text{div}(J_p) \quad (2)$$

- Equations of currents:

$$J_n = q\mu_n nE + \mu_n KT \frac{\partial n}{\partial x} \quad (3)$$

$$J_p = q\mu_p pE - \mu_p KT \frac{\partial p}{\partial x} \quad (4)$$

3.1.1 Calculation of the current in the MPP layer (n)

This layer gives us a photohole (I_p) expressed by the equation (7).

- Boundary conditions:

$$S_p \Delta p = D_p \left. \frac{\partial \Delta p}{\partial x} \right|_{x=0} \quad (5)$$

$$\Delta p \Big|_{x=x_j} = 0 \quad (6)$$

$$J_p = \frac{q\alpha_1 L_p \Phi_i (1-R)}{(\alpha_1^2 L_p^2 - 1)} \left[\frac{\left(\frac{S_p L_p}{D_p} + \alpha_1 L_p \right) \exp(-\alpha_1 x_j) \left(\frac{S_p L_p}{D_p} \cosh\left(\frac{x_j}{L_p}\right) + \sinh\left(\frac{x_j}{L_p}\right) \right)}{\frac{S_p L_p}{D_p} \sinh\left(\frac{x_j}{L_p}\right) + \cosh\left(\frac{x_j}{L_p}\right)} - \alpha_1 L_p \exp(-\alpha_1 x_j) \right] \quad (7)$$

$$L_p = L_{MPP} \quad (8)$$

3.1.2 Calculation of the current in ZnPc layer (p)

This zone presents the donor; it gives us a photoelectron (In).

- Boundary conditions:

$$S_n \Delta_n = D_n \left. \frac{\partial \Delta n}{\partial x} \right|_{x=h} \quad (9)$$

$$\Delta n \Big|_{x=x_j + L_{MPP} + L_{ZnPc}} = 0 \quad (10)$$

$$J_n = \frac{q\Phi_i (1-R) \exp(-\alpha_1 (x_j + L_{MPP})) \exp(-\alpha_2 L_{ZnPc}) \alpha_2 L_n}{(\alpha_2^2 L_n^2 - 1)}$$

$$\left[\frac{\frac{S_n L_n}{D_n} \left(\cosh\left(\frac{x_b}{L_n}\right) - \exp(-\alpha_2 x_b) \right) + \sinh\left(\frac{x_b}{L_n}\right) + \alpha_2 L_n \exp(-\alpha_2 x_b)}{\frac{S_n L_n}{D_n} \sinh\left(\frac{x_b}{L_n}\right) + \cosh\left(\frac{x_b}{L_n}\right)} \right] \alpha_2 L_n \quad (11)$$

$$L_n = L_{ZnPc} \quad (12)$$

$$x_b = h - (x_j + L_{MPP} + L_{ZnPc}). \quad (13)$$

3.1.3 The current in the active area (Ig)

The excitons generated in the active region (in the vicinity of the interface) are effective on the level of dissociation (production of the carriers), therefore, the photocurrent in this zone is:

$$J_g = q\Phi_i (1-R) \exp(-\alpha_1 x_j) \left[(1 - \exp(-\alpha_1 L_{MPP})) + \exp(-\alpha_1 L_{MPP}) (1 - \exp(-\alpha_2 L_{ZnPc})) \right] \quad (14)$$

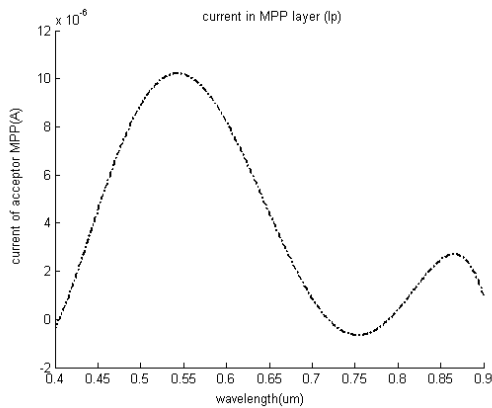


Fig. 5: Variation of the current of MPP layer according to the wavelength.

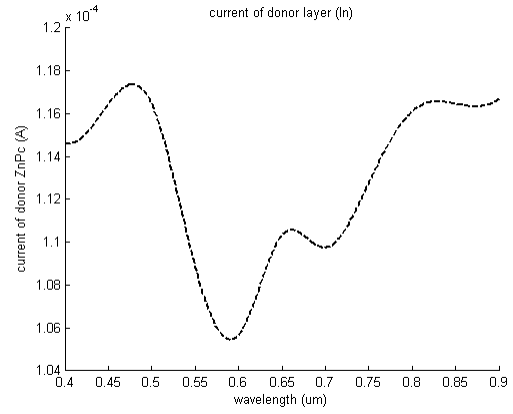


Fig. 6: Variation of the current of ZnPc layer according to the wavelength.

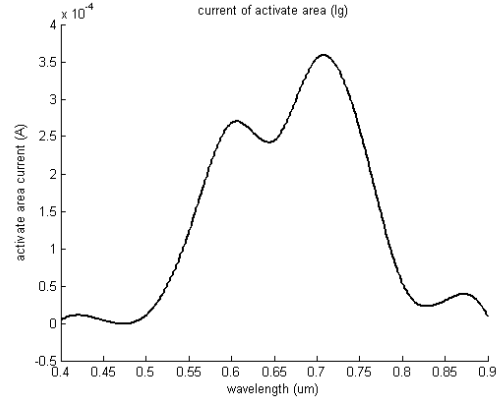


Fig. 7: Variation of the current of the activate area according to the wavelength.

(Fig. 7) shows interesting values of the photocurrent in the active area. This photocurrent is considerable compared with the photocurrents of layers MPP and ZnPc (Fig. 5) and (Fig. 6); it is about mA on a layer thickness of 6 nm. Comparing with the current in the ZnPc area, this last is comparable but the thickness of this layer is also larger (220 nm). The photocurrent of the active zone sweeps the interval of 500-800 nm and the maximum is around 700 nm.

These results affirm us that the principal generation of the photocurrent is localised in the active area, which presents a very fine area by contribution with the thicknesses of the donor layer and acceptor. Thus, the excitons generated in the active area (in the vicinity of the interface) are effective on the level of dissociation (production of photocurrent).

3.2. Characteristic I(V)

The equivalent electric circuit is given by (Fig. 8), where $R_s = R_{ITO} + R_{ZnPc} + R_{MPP} + R_{ITO}$.

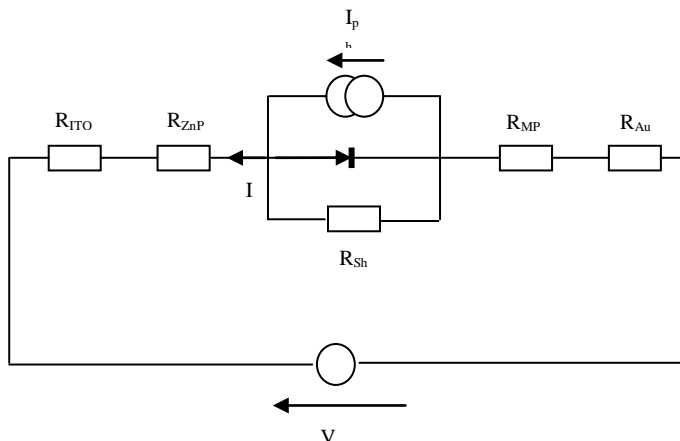


Fig. 8: Electric circuit of the MPP/ZnPc cell [23].

According to this equivalent circuit, we deduced the equation characteristic I (V) of the cell:

$$I(V) = I_{ph} - I_s \left[\exp\left(\frac{V + R_s I}{U_T}\right) - 1 \right] - \frac{V + R_s I}{R_{Sh}} \tag{15}$$

The (Fig. 9) represent the I(V) characteristic, the conversion efficiency and the file factor is given in (Table 1).

Table 1: Double-layer structural features MPP/ZnPc.

$I_{sc}(mA/cm^2)$	$V_{co}(mV)$	$\eta(\%)$	FF(%)
2.6	266.2	0.72	51.71

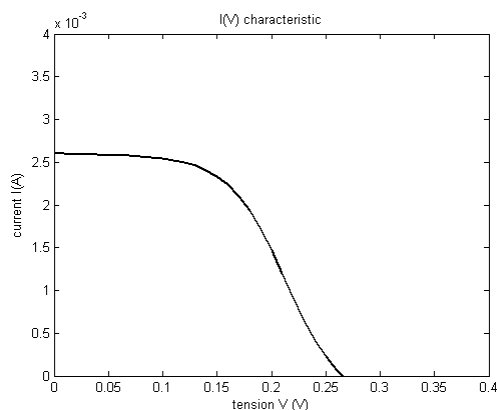


Fig.9: I(V) characteristic for the MPP/ZnPc structure.

3.2. 1. Insertion of the composite layer ZnPc/C60

For an improvement of the performances of the double-layer cell MPP/ZnPc, we needs an increase thickness of the interfacial zone to resolve the problem of the recombinations due to the no dissociation of excitons create far from the interface of the heterojunction.

For this reason a layer made up of a mixture of C60 and ZnPc (1:1) is inserted between ZnPc and the MPP thickness of 30 nm.

The value of the calculated photocurrent increases the 2,6 mA to 5,3 mA [23]. The (Fig. 10) shows I(V) characteristic for this structure improved and a comparison with experimental results [23]. The (Table 2) summarize the characteristics of this structure.

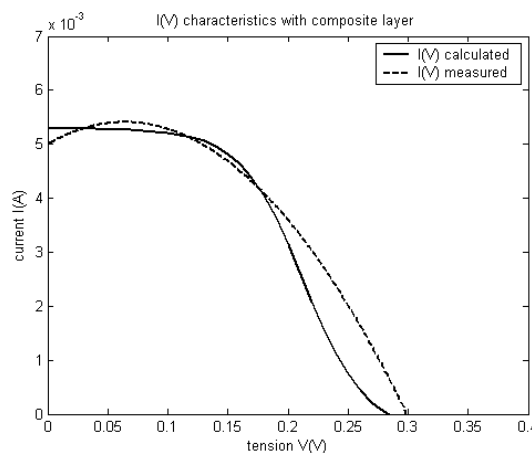


Fig. 10 : I(V) characteristic for the MPP/ZnPc structure contains the composite layer ZnPc/C₆₀ (1:1).

Table 2: Performances of the double-layer structure MPP/ZnPc with the composite layer ZnPc/C₆₀.

$I_{sc}(mA/cm^2)$	$V_{co}(mV)$	$\eta(\%)$	FF(%)
5.3	286.5	1.49	49.31

4. Conclusion

Until now the results obtained for organic solar cells either experimental or are based on statistical statements starting from the spectral answers of the cells. We worked out a numerical model based on the resolution of the equations of continuities who gave the results in good accordance with literature and which allowed, moreover a better control of the performances of the organic cells, for their improvement.

5. References

[1] R.H. Friend, R.W. Gymer, A.B. Holmes, J.H. Burroughes, R.N. Marks, C. Taliani, D.D.C. Bradley, D.A. Dos Santos, J.L. Brédas, M. Lögdlund, W.R. Salaneck, Nature. 397, pp. 121, 1999.

[2] A. J. Mozer, N.S. Sariciftci, 'Conjugated polymer photovoltaic devices and materials', C. R. Chimie, 9, pp. 568-577, 2006.

[3] B.J.Land, R.P.Raffaella and all, prog. Photovolt: Res.Appl, 13, pp. 165-172, 2005.

[4] A. K. Ghosh, T. J. Feng, J. Appl. Phys, 49, pp. 59-82, 1978.

[5] Dhritiman Gupta, Sabyasachi Mukhopadhyay, K. S. Narayan, 'Fill factor in organic solar cells', Solar Energy Materials & Solar Cells, 2008.

- [6] C. W. Tang, 'Two-layer organic photovoltaic cell', *Appl. Phys. Lett*, 48, (2), pp. 183-185, 1986.
- [7] K. Seki, N. Hayashi, H. Oji, E. Ito, Y. Ouchi, H. Ishii, *Thin Solid Films*, 393, pp. 298, 2001.
- [8] S. Gunes, H. Neugebauer, N. S. Sariciftci, 'Conjugated Polymer-Based Organic Solar Cells', *Chem. Rev*, 107, (4), pp. 1324-1338, 2007.
- [9] M. Oukchmih, 'Les cellules photovoltaïques a base de matériaux organiques discotiques', Ph.D. Thesis, Laboratoire de Génie Electrique de Toulouse, Univ-Paul Sabatier, 2003.
- [10] B. Brousse, 'Réalisation et caractérisation de cellules photovoltaïques organiques obtenues par dépôt physique', Ph.D. Thesis, Ecole doctorale Sciences - Technologie - Santé, Faculté de Sciences et Technique de Limoges, Univ-Limoges, 2004.
- [11] J. Rostalski, D. Meissner, 'Photocurrent spectroscopy for the investigation of charge carrier generation and transport mechanism in organic p/n-junction solar cells', *Solar Energy Materials & Solar Cells*, 63, pp. 37-47, 2000.
- [12] J. Rostaski, D. Meissner, 'Monochromatic versus solar efficiencies of organic solar cells', *Sol. Energy Mater. Sol. Cells*, 61, pp. 87-95, 2000.
- [13] P. Peumans, A. Yakimov, S.R. Forrest, 'Small molecule weight organic thin-film photodetectors and solar cells', *J. Appl. Phys*, 93, (7), pp. 3693, 2003.
- [14] Halls, Pichler, Friend, Moratti, Holmes, 'Exciton dissociation at a PPV / C60 heterojunction', *Synthetic Metals*, 77, pp. 277-280, 1996.
- [15] Lee, Khabibullaev, Zakhidov, Morita, Yoshino, 'Photovoltaic properties of C60 / PPP heterojunction: molecular D - A photocell', *Synthetic Metals*, 71, pp. 2247-2248, 1995.
- [16] H. Jin, Y. Xianguo, 'Enhanced photovoltaic properties of polymer- fullerene bulk heterojunction solar cells by thermal annealing', *Solid state communication*, 142, pp. 181-184, 2007.
- [17] X. Meng, F. Teng, 'Electric field induced quenching of photoluminescence in the MEH-PPV: C₆₀', *Chemical physics lett*, 443, pp. 374-377, 2007.
- [18] Onada, and Tada: 'Photovoltaic effects of MDOPPV / PPy layer', *Thin Solid Films*, 393, pp. 284-290, 2001.
- [19] S. Bertho, I. Haeldermans and all, 'Influence of thermal ageing on the stability of polymer bulk heterojunction solar cells', *Solar Energy Materials & Solar Cells*, 91, pp. 385-389, 2007.
- [20] G. Li, V. Shrotriya, J. Huang, Y. Yao, T. Moriarty, K. Emery, Y. Yang, 'High-efficiency solution processable polymer photovoltaic cells by self-organization of polymer blends', *Nature Materials*, 4, pp. 864-868, 2005.
- [21] W. Ma, C. Yang, X. Gong, K. Lee, A. J. Heeger, 'Thermally Stable, Efficient Polymer Solar Cells with Nanoscale Control of the Interpenetrating Network Morphology', *Adv. Funct. Mater*, 15, (10), pp. 1617-1622, 2005.
- [22] M. Reyes-Reyes, K. Kim, J. Dewald, R. Lopez-Sandoval, A. Avadhanula, S. Curran, D. L. Carroll, 'Meso-Structure Formation for Enhanced Organic Cells', *Organic Letters*, 7, (26), pp. 5749-5752, 2005.
- [23] D. Meissner, J. Rostaski, 'Highly Efficient Molecular Organic Solar Cells'. in: *Proc. 16th European photovoltaic solar energy conf*, Glasgow, United Kindom, vol. 3, pp. 10-14, May 2000.

I-V Characteristics Model For AlGa_N/Ga_N HEMTs Using Tcad-Silvaco

Abdelmalek Douara^a, Bouaza Djellouli^b, Abdelaziz Rabehi^c, Abderrezak Ziane^c and Nabil Belkadi^c

^a Applied Materials Laboratory, Research Center, University Djillali Liabes of Sidi Bel Abbes, 22000 Sidi Bel Abbes, Algeria

^b Laboratory of Modelling and calculation Methods LMCM, 20002 University of Saida, Algeria

^c Applied Microelectronics Laboratory, University Djillali Liabes of Sidi Bel Abbes, 22000 Sidi Bel Abbes, Algeria

Received date: May 25, 2014; revised date: December 09, 2014; accepted date: December 21, 2014

Abstract

We report some results the drain current characteristics of AlGa_N/Ga_N HEMT (High Electron Mobility Transistor). on are simulated by changing the different device parameters such as Al content x and the barrier thickness for different values of the gate voltage using Tcad-Silvaco numerical simulation software. Drift-diffusion model has taken for simulating the proposed device. we use SiC as a substrate for this structure. The channel is made of Ga_N and source-drain spacing is 1 μm .

Keywords: AlGa_N/Ga_N, HEMT, Tcad-Silvaco;

1. Introduction

The active components are the basic elements of the design of microwave monolithic integrated circuits. The active elements are formed of transistors and diodes. Today, we must design transistors and diodes capable of meeting the requirements in terms of power and increase in frequency [1] [2] [3].

The III-N semiconductor materials are good candidates for the fabrication of these types of transistors and diodes. The III-N semiconductor materials have several advantages such as a wide bandgap, a high chemical stability, and exceptional physical properties other outstanding mechanical properties. These semiconductors possess the necessary qualities to make power components.

Thus, since many years, the industry uses microwave technology HEMT. Until now, the transistors are HEMTs formed in a die Gallium nitride (Ga_N). However, Ga_N and other materials such as silicon are used too close to their ultimate physical limitations, especially at the power densities supplied.

2. AlGa_N/Ga_N HEMT STRUCTURE: 2-DEG Formation & Polarization effect

The basic concept in a HEMT (Fig.1) is the aligning of a wide and narrow bandgap semiconductor adjacent to each other to form a heterojunction. The carriers from a doped wide energy gap material (AlGa_N) diffuse to the narrow band gap materials (Ga_N) where a dense 2-DEG (Two Dimensional Electron Gas) is formed in the Ga_N side but close to the boundary with AlGa_N.

The unique feature of the HEMT is channel formation from carriers accumulated along a grossly asymmetric heterojunction, i.e. a junction between a heavily doped high bandgap and a lightly doped low bandgap region [4].

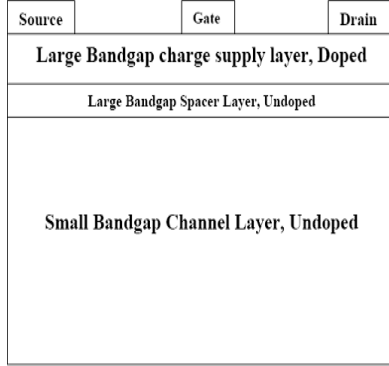


Fig 1: Layered structure of High Electron Mobility Transistor.

To achieve proper operation of the device, the barrier layer $\text{Al}_x\text{Ga}_{1-x}\text{N}$ must be at a higher energy level than the conduction band of the GaN channel layer. This conduction band offset transfers electrons from the barrier layer to the channel layer. The electrons that are transferred are confined to a small region in the channel layer near the hetero-interface. This layer is called the 2DEG (Fig.2) and a defining characteristic of the HEMT. There are many factors that determine the quality of the 2DEG.

The factors involved in the development of the 2DEG are type of substrate, growing method, and level of doping of the carrier supply layer [8].

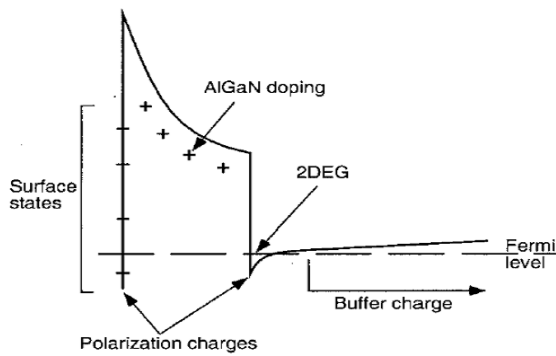


Fig 2: Energy band diagram showing 2DEG formation.

2.1. Current- Voltage Characteristics

The Current-Voltage is related to the density variation for the 2DEG density under the influence of a gate-source voltage applied of the component. In fact, any action on the gate voltage V_{gs} has the effect to modify the electronic population of the channel which varies the electrons density n_s . Several authors have developed models in order to account for the $I_{DS}(V_{DS})$ characteristics electrical behavior of HEMTs [9][6]. First, we started to introduce conventional expression of the drain-source current I_{DS} according to the voltage drain-source V_{DS} in order to determine ideal characteristics $I_{DS}(V_{DS})$ for different values of V_{gs} . The current I_{DS} is proportional to the density of electrons in the channel n_s which is expressed as follows [7][5]:

$$I_{DS}(x) = W \mu_n q n_s E(x) \quad (1)$$

where W is the channel width and μ_n is the mobility of carriers.

Since the current is constant throughout the channel, integrating the above equation from source to -drain gives:

$$I_{DS} = W \mu_n C_0 / L \left[(V_G - V_{th}) V_{DS} - \frac{V_{DS}^2}{2} \right] \quad (2)$$

The output characteristics for an enhancement - mode HEMT are shown in Fig 3. In the linear region where $V_{DS} \ll (V_G - V_{th})$, Eq (2) is reduced to an ohmic expression:

$$I_{lin} = \frac{W \mu_n C_0 (V_G - V_{th}) V_{DS}}{L} \quad (3)$$

from the equation (3), the transconductance can be obtained as follow :

$$g_{m,lin} \equiv \frac{dI_{lin}}{dV_G} = \frac{W \mu_n C_0 V_{DS}}{L} \quad (4)$$

At high V_{DS} , n_s at the drain is reduced to zero, corresponding to the pinch-off condition an current saturates with V_{DS} .

3. Results

3.1. simulation model

In this model, we use SiC as a substrate for HEMT structures AlGaN/GaN. The fig 3 shows a schematic representation of the HEMT structure in two dimensions. The channel is based not intentionally doped GaN (nid). The doping concentration in this layer is $N_{D1} = 10^{15} \text{ cm}^{-3}$ of type N, the channel width is 10 nm. The channel is inserted between two spacer layers of thickness 55 nm with a doping $N_{D2} = 10^{17} \text{ cm}^{-3}$ in which is inserted a δ doping layer with $N_{D2} = 2 \times 10^{18} \text{ cm}^{-3}$. The device at a gate length of 0.6 microns and a source-drain spacing is 1 micron.

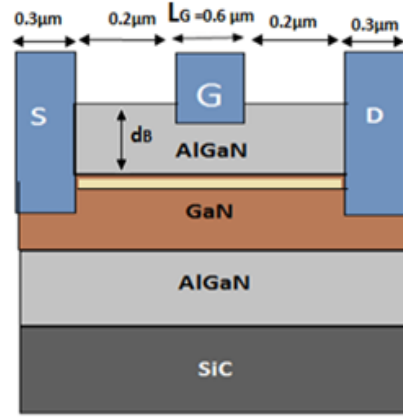


Fig 3: A scheme simulating an HEMT AlGaN / GaN two-dimensional

3.2. $I_{DS} (V_{DS})$ Characteristics for different values of molar fraction (x)

The current-voltage characteristics of a HEMT transistor based heterostructure AlGaN/GaN are shown in figure 4 . These results are obtained by varying the drain voltage for different values of the voltage V_{GS} applied to the gate and the two values of "x" molar fraction.

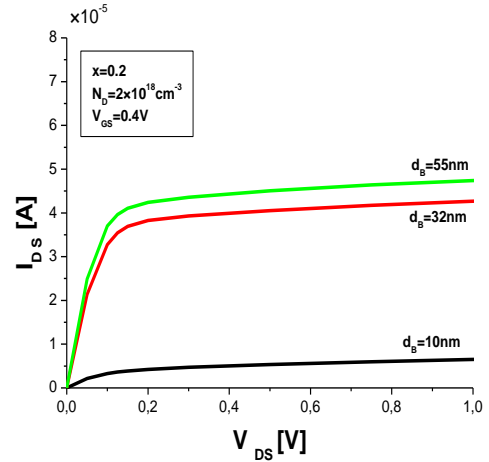
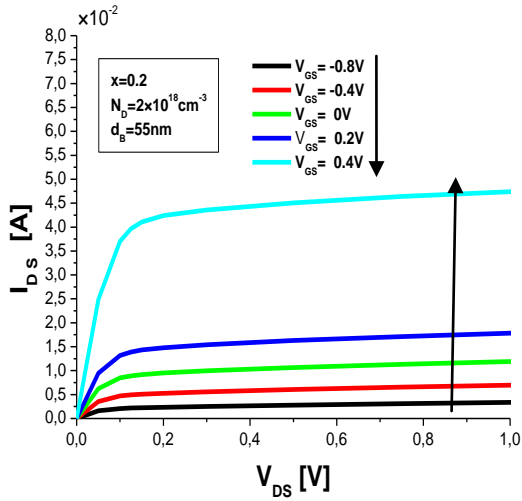


Fig 5: Evolution of the drain-source "Ids" depending on the drain voltage "Vds" for different values of the thickness "db".

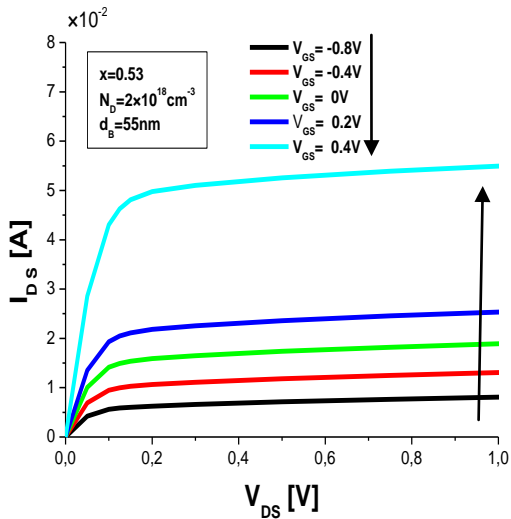


Fig 4: Evolution of the drain-source "Ids" depending on the drain voltage "Vds" for different values of the gate voltage in the effect of x.

3.4. Ids (Vds) Characteristics for different values of gate width (Lg) at Vgs = 0.4V

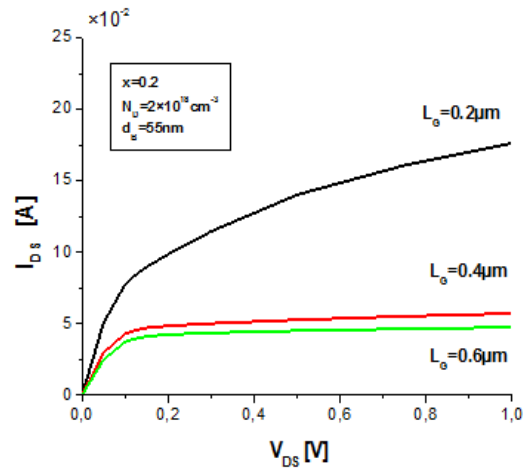


Fig 6 : Evolution of the drain-source "Ids" depending on the drain voltage "Vds" for different values of the gate width "Lg".

3.3. Ids (Vds) Characteristics for different values of barrier thickness (db)

3.5. $I_{DS}(V_{DS})$ characteristics for different values of temperature (T)

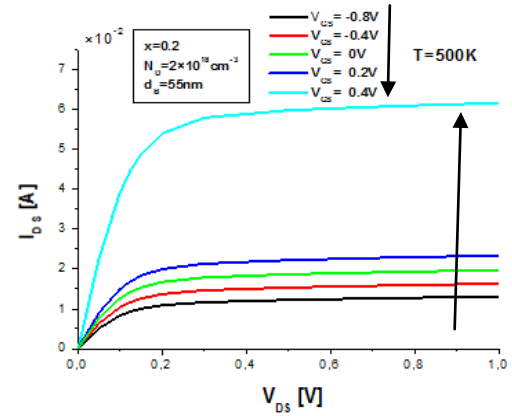
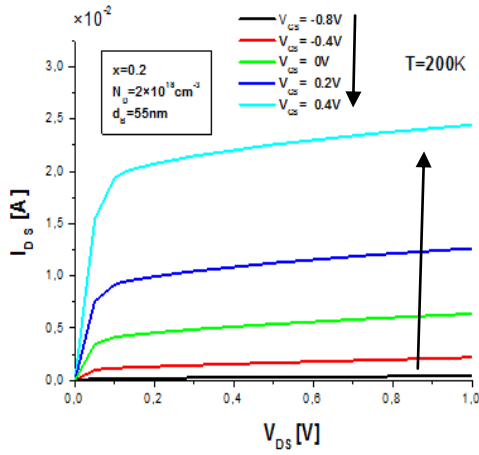
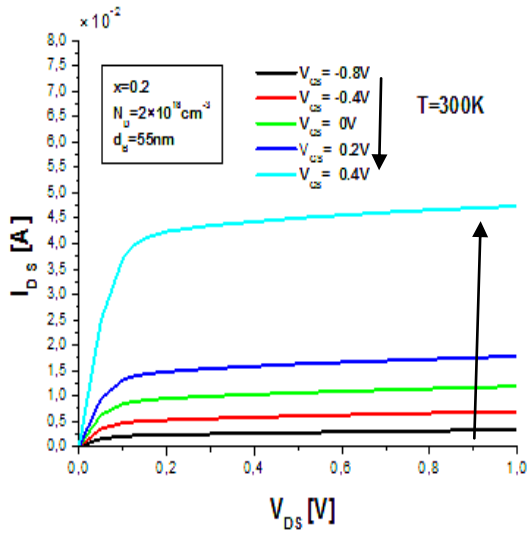


Fig 8: $I_{DS}(V_{DS})$ characteristics for different V_{GS} with thermal effect



4. Conclusion

we have presented the results of $I_{DS}(V_{DS})$ characteristic of HEMT AlGaIn/GaN 2D with Silvaco ATLAS software and concerns that the effect of some physical parameters and geometry to improve the performance of transistor among them (the aluminum content (x), the gate width (L_G) ... etc.).

It was found that the intensity of drain-source current value to $I_{DS} = 0.065A$. But we note that the effect of languor grid is very important compared with other parameters to increase the current value for $L_G = 0.2 \mu\text{m}$ intensity rises to $I_{DS} = 0.16A$.

References

[1] S. de Mayer, « Etude d'une nouvelle filière de composants HEMTs sur technologie nitrure de gallium. d'amplificateur distribué de puissance à très large bande. »
Doctoral thesis on 12 Septembre 2005, Limoges University.

[2] N. Ghalichechian, « Silicon Carbide Overview Physical Properties and Thin Film Deposition». ENEE793, Solid State Electronics Fall 2002.

[3] S.M. Sze, «Semiconductor Devices - Physics and Technology». 1985, ISBN 0-471-87424-8.

[4] S. Tzeng, "Low-Frequency Noise Sources in III-V Semiconductor Heterostructures," 2004.

[5] Rashmi, A. Kranti, S. Haldar, M. Gupta and R. S. Gupta, "An Accurate Charge Control Model for Spontaneous and Piezoelectric Polarization Dependent Two-Dimensional Electron Gas Sheet Charge Density of Lattice-Mis-matched AlGaIn/GaN

HEMTs," Solid-State Electronics, Vol. 46, No. 5, 2002, pp. 621-630.

[6] E.W. Faraclas and A. F. M. Anwar, "AlGaIn/GaN HEMTs: Experiment and Simulation of DC Characteristics," Solid-State Electronics, Vol. 50, No. 6, 2006, pp. 1051-1056.

[7] I. Saidi, M. Gassoumi, H. Maaref, H. Mejri and C. Gaquière, "Self-Heating and Trapping Effects in

[8] P. Javorka, "Fabrication and Characterization of AlGaIn/GaN High Electron Mobility Transistors." 2004.

[9] X. Cheng, M. Li and Y. Wang, "An Analytical Model for Current-Voltage Characteristics of AlGaIn/GaN HEMTs in Presence of Self-Heating Effect," Solid-State Electronics, Vol. 54, No. 1, 2010, pp. 42-47.

AlGaIn/GaN Heterojunction Field-Effect Transistors," Journal of Applied Physics, Vol. 106, 2009, pp. 1-7.

Simulation of the carbon nanotubes in the terahertz frequencies

Chahrazed Dridi and Mourad Zaabat

Laboratory of Actif Component and Materials,
Sciences Faculty, Oum El Bouaghi University, 04000, Algeria

Received date: May 25, 2014; revised date: December 10, 2014; accepted date: December 21, 2014

Abstract

Since little is known isolate a sheet of carbon-graphite one atom thick. This crystal is two-dimensional graphene has remarkable electronic transport properties, which are neither those of a metal nor those of a semiconductor. In this paper we have developed a novel structure electromagnetic bandgap (EBG), with a periodic arrays of carbon nanotubes presented, by introducing a multiwalled carbon nanotubes like a metallic viaholes. The electromagnetic bandgap (EBG) surface, also referred to as a photonic bandgap (PBG) surface, has attracted extensive studies, In the optical domain, microwave and millimeter-wave areas [1]. The method used is an integral method based on the concept of waves (WCIP).

Keywords: carbon nanotubes, EBG structure, wcip method

1. Introduction

Molecular electronics is an emerging nano physics, promising to make new types of devices useful for both information storage quantum information. Among the nanostructures considered for the construction of a molecular electronics, the carbon nanotube is presented as a particularly promising candidate.

Since the articles reference S.Iijima early 90s, carbon nanotubes have been extensively characterized and found to be very interesting for the development of nanoelectronics due to their many remarkable properties. Nanotubes are nanometer diameter cylinders micron length, which can be seen as the winding of a sheet of graphite.

Their cylindrical shape and the particular electronic structure resulting make a rare experimental realizations of one-dimensional electronic system. The carbon nanotube is characterized by the helicity and the diameter of the tube, since these two parameters determine the periodic boundary conditions of the electronic wave functions.

In this work we develop a new iterative method based on wave concept (WCIP) to model a forest of multiwalled carbon nanotubes (MWCNT) fig-1.

2. Method and formulation

Multiwall carbon nanotubes sheet (MWCNT) consist of multiple graphene sheet (2 to 50) rolled

around each other. For this work, we chose multiwalled carbon nanotubes with diameters around of 2 and 25 nm.

The periodic structure have attracted much attention in recent years for promising application in the fields microelectronics, in this context and in order to respond to new needs of the modeling of planar circuits integrants passive elements that this work is situated.

Our approach will focus on the global modeling of periodic structure designed by carbon nanotubes, we introduce the iterative method denoted WCIP who is an integral method based on the concept of wave for solving electromagnetic scattering problems and analysis of planar circuits, it appeals to the fast fourier transform mode (FMT).

The passage between the spatial domain and the spectral domain is obtained by a 2D-FFT (also called Fast Modal Transform). This method depends on the manipulation of incident and reflected waves instead of electromagnetic field [2], [3].

Thus, method defines two operators in the spectral and spatial domain.

WCIP method uses easy equations to solve that with the integral method.

The main characteristic of periodic structures is to act as a device band-stop to remove undesirable electromagnetic waves in a certain frequency range Fig-1.

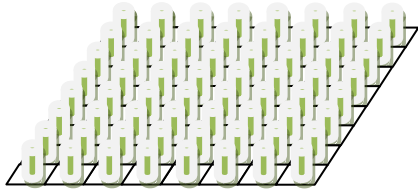


Fig-1 structure with via holes carbon nanotubes

The writing of electric field E_i and surface current density J_i in terms of incident and reflected waves are given by the following set of equations [2]:

$$E_i = \sqrt{Z_{0i}}(A_i + B_i) \quad J_i = \frac{1}{\sqrt{Z_{0i}}}(A_i - B_i) \quad (1)$$

Where:

A_i and B_i are two tangential vectors associated with the discontinuity interface Ω Fig-2.

J_i is the surface tangential current density.

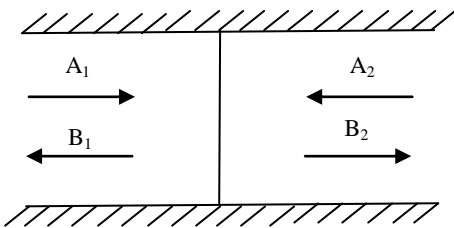
E_i is the tangential electric field.

Z_{0i} is the intrinsic impedance of the two middles.

The nanotube structure is determined by the pair of integers (m, n) defining a feature vector of the winding called vector of chirality[4] [5]:

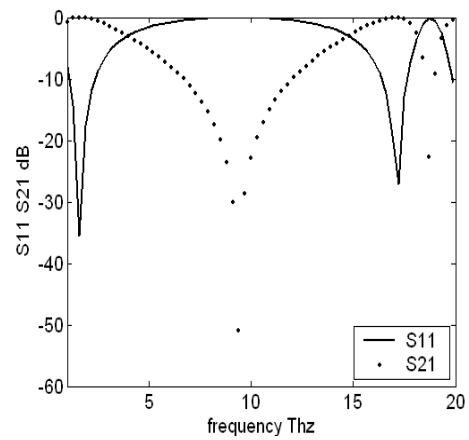
$$\vec{C}_h = n\vec{a}_1 + m\vec{a}_2$$

$$d_t = \frac{C_h}{\pi} = a_{c-c} \frac{\sqrt{3}\sqrt{(n^2+nm+m^2)}}{\pi}, \quad a_{c-c} = 1.42 \text{ \AA} \quad (2)$$

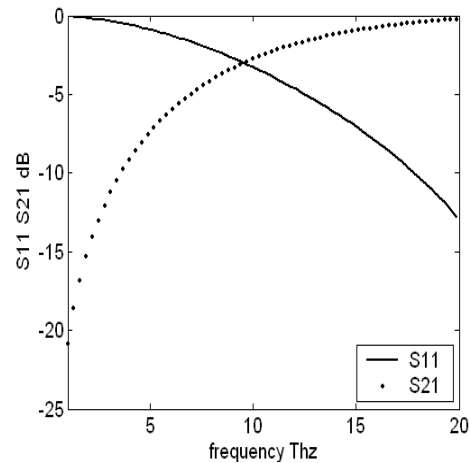
Fig-2 Illustration of waves on both sides of the interface Ω

3. Application

In this study we present the influence of the number of carbon nanotubes(via holes) on the response of S-parameters and the influence of the distance between carbon nanotubes , to do this we chose to work with the number N of carbon nanotubes variant. The structure of geometric dimensions $a = b = 36\mu\text{m}$, the length of the carbon nanotube $L = 16\mu\text{m}$ and a diameter of 25nm Fig-4.



(a)



(b)

Fig-3 Scattering parameters for ($L = 16\mu\text{m}$) and ($L=1\mu\text{m}$).

Fig-3 (a) shows the S-parameters as function of the frequency according to a structure formed by 1024

via holes the length of the via hole $L = 16\mu\text{m}$ and Fig-3 (b) shows the scattering parameters for $1\mu\text{m}$ of length.

We note in Fig-3 (b) no resonances in the frequency range of 2-20 THz this implies that more the length of the hole is small and more the resonant frequencies are away to above 20 THz values.

On Fig-4, we have the Scattering S parameters variation depending on the number of nanotubes present in the structure, however this number only affects the bandwidth so the diameter and the length of carbon nanotube can be considered as filter criteria.

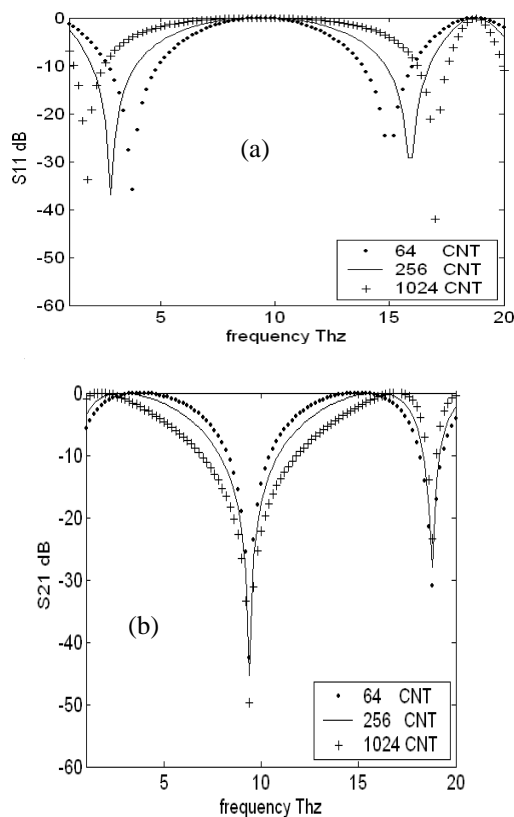


Fig-4 Scattering parameters with variant number of nanotubes

4. Conclusion

In this article the EBG structure based on carbon nanotubes is characterized by an efficient numerical method based on wave concept iterative process (WCIP), mostly used for planar circuits. The simulation results obtained confirm that the parameters of the studied structure are filtering criteria.

References

- [1] D. Sievenpiper, L. Zhang, R. F. J. Broas, N. G. Alexopolous, and E. Yablonovitch, "High-impedance electromagnetic surfaces with a forbidden frequency band," *IEEE Trans. microwave Theory & Tech.*, vol. 47, pp. 2059-2074, Nov. 1999.
- [2] A. Gharsallah, A. Gharbi and H. Baudrand, "Efficient analysis of multiport passive circuits using iterative technique," *Electromagnetics*, vol. 21, 2001, pp. 73-84.
- [3] H. Baudrand, R.S. N'gongo, "Applications of wave concept iterative procedure", *Recent RE. Devel. Microwave an Tech vol 1*, pp 187-197, 1999.
- [4] Dresselhaus, M. S., Dresselhaus, G., and Eklund, P. C., 1996, *Science of Fullerenes and Carbon notubes* (New York: Academic Press).
- [5] Saito, R., Dresselhaus, G., and Dresselhaus, M. S., 1998, *Physical Properties of Carbon Nanotubes* (London: Imperial College Press).

3D Numerical simulation of a dual metal (Aluminum, Titanium) horizontal square surrounding gate MOSFET

Mohammed Khaouani^{a,b}, Ahlam Guen Bouazza^{a,b}, Benyounes Bouazza^{a,b} and Zakarya Kourdi^{a,b}

^aUniversity, Abou Bekr Belkaïd of Tlemcen Faculty of Technology BP230 Tlemcen 13000(Algéria)

^bURMER Research Unit

Received date: May 25, 2014; revised date: December 11, 2014; accepted date: December 21, 2014

Abstract

Essentially due to the uninterrupted scaling of MOSFET transistors, it has become absolute obligatory to explore for new transistors architectures in order to reach better control of short channel effects. Also the integrity and issues related to electrostatic performance associated with scaling Silicon MOSFET bulk sub 10 nm channel length promotes research in new device architectures such as SOI, double gate and gate all around GAA MOSFETs [1]. In literature GAA structure has been proposed to reduce the SCEs due to scaling of the MOSFET transistor. GAA structures, that are actually strong candidates for the next generation nanoscale devices, show an even stronger control of short channel effects.

In this paper, a double metal square surrounding gate MOSFET for reduces short channel effects is presented. Our results take into account quantum confinement. In the latter part of the paper some 2D simulation results of our structure has been shown using SILVACO TCAD tools. We will also exhibit some simulation results we obtained relating to the influence of some parameters variation on our structure, that have a direct impact on their threshold voltage and drain current. In addition, our Transistor showed reasonable Ion/Ioff ratio of (10⁶) and low drain induced barrier lowering (DIBL) of 39mV/V

keywords: GAA ; SILVACO-TCAD ; quantum effects ; MOSFETs; dual metal.

1. Introduction

During the last decade, Field-Effect transistors have legitimate chipmakers to shrink these devices to only tens of nanometres in length designing new MOSFETs architectures. Indeed, as transistors become smaller, physical limitations of current planar transistors appears. MUGFET Si-based devices such as gate-all around (GAA) MOSFETs seem to be are very promising candidates for aggressively scaled CMOS, and can potentially solve various problems with scaling down the size of transistors . These problems include the electron tunneling due to thinner layers of the insulating barriers, the increased threshold leakage that comes with shorter channel length, and the corner effects produced by smaller sized and square corners. GAA transistors presented in this study own an excellent electrostatics, low power consumption, immunity to short channel effects that plays important role in devices, drain induced barrier lowering, handling out of the gate, and the reduction of leakage current [2],[3].

However beyond the 10 nm range, quantum confinement must be considered. These effects have been included in several books related to the square GAA JLFETs [4] [5], but none of quantum effects has been modeled in extremely devices - scale ,where quantum confinement effects become important and governing the performance of the device. The GAA MOSFET, which is basically a 3-D structure, cannot be analyzes directly the same way. One possibility is to solve Laplace's equation in rectangular coordinates by means of a series expansion in Bessel functions [6] and then Bohm quantum potential (BQP) model used in simulations allows to calculate a position dependent potential energy term using an auxiliary equation derived from the Bohm interpretation of quantum mechanics. This extra concentration is integrated in the whole structure and then this quantity is derived as $C=dQ/dV$ [7].

In this paper, 3D quantum numerical simulation a double metal square surrounding gate MOSFET, that is a quadruple gate with square section , have been validated using SILVACO TCAD simulations in order to present some interesting characteristics and the influence of some parameters variation on our

structure, that having a direct impact on their drain current [8],[9].The threshold voltage is analyzed for device parameters such as gate length ratios, oxide thickness, silicon thickness, and doping concentration.

2. Device design

Our 3D device has been generated using SILVACO TCAD tools and is shown in figure1. The different parameters of our structure are assumed as follows: Gate Length of 9 nm, a lightly doped channel region $1.0E+17/cm^3$ (Boron) so that there is substantially no degradation of mobility due to channel doping, heavily doped drain and source regions (Arsenic) $1E20/cm^3$, silicon dioxide with 1 nm thickness used as gate oxide allows to stop the gate tunneling current, dual metal gate aluminum are considered with $\phi_{M1} = 4.1$ eV for aluminum and $\phi_{M1} = 4.4$ eV for Titanium , the height and width of our device are $W=H=5nm$. As shown in Figure 1 our Gate-all-around FETs square looks like FinFETs excluding that the gate material surrounds the channel region on all sides.

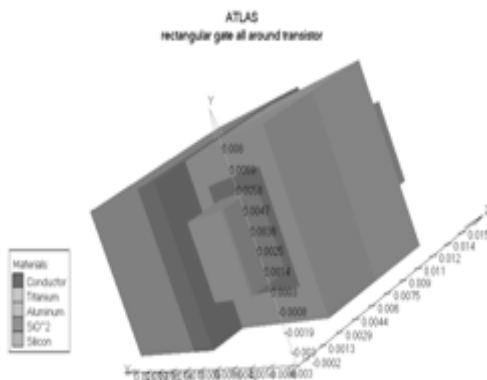


Figure.1 3D view of a dual metal square surrounding gate MOSFET.

3. Results

Our results have been validated using numerical simulation that is an extremely helpful tool for detailed investigation of physical phenomena, which determine electrical characteristics of semiconductor devices [8],[9]. In this study Atlas Silvaco Software has been chosen [10]. The simulated output and transfer

characteristics of the GAA device considered are plotted in figures 2 and 3.

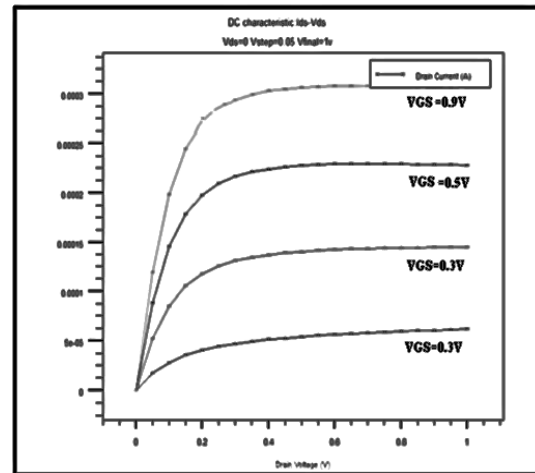


Figure. 2 ID versus VD characteristics

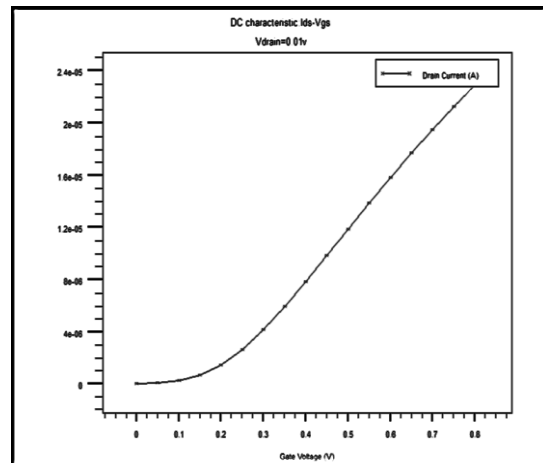


Figure.3 Transfer characteristic

Figure 2 shows IV characteristics of our square GAA with n-type semiconducting channel at different positive gate bias. In contrast, Figure 3 shows transfer characteristic of our device. Threshold voltage can be extracted from this figure knowing that physically, the threshold voltage is defined as the gate voltage that is required for creating a conducting channel and allowing the carriers to flow from the electrode source to the drain crossing this conducting channel. In our case threshold voltage extracted V_{th} is equal to 120mV. In order to study the influence of the studied structure parameters on our device electrical characteristics, some physical and geometrical

parameters are modified. We examine then the effect of each parameter variations on our GAA transistor drain current and threshold voltage .

3.1. Influence of T_{ox} variation on I_D current and threshold voltage V_{th}

Figure 4 shows our device output characteristics at different oxide thickness.

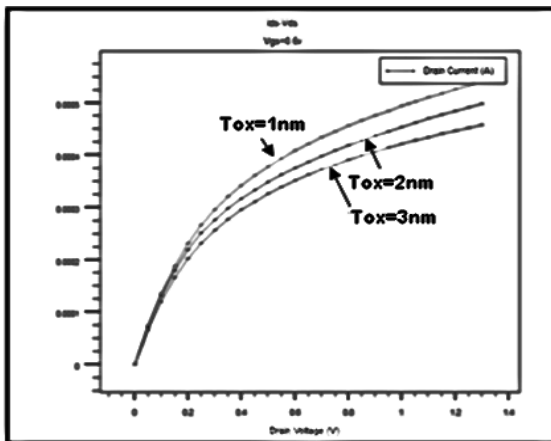


Figure.4 Output characteristics for a dual metal gate GAA MOSFETs at different oxide thickness ($T_{ox}=1\text{nm}$, 2nm , 3nm).

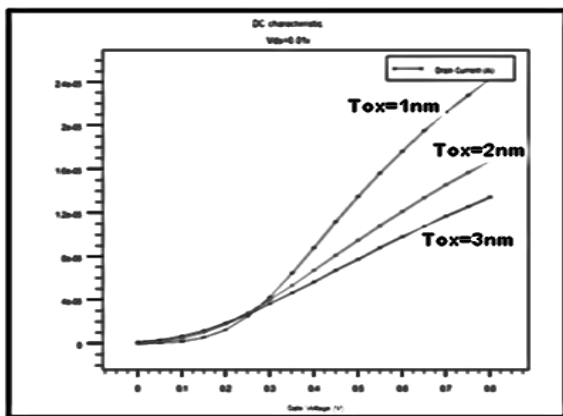


Figure.5 Transfer characteristics for a dual metal gate GAA MOSFETs at different oxide thickness ($T_{ox}=1\text{nm}$, 2nm , 3nm).

We can observe that drain saturation current increases at shorter oxide thickness. We can conclude for this variation that thinner gate oxides lead to product higher drain currents. Figure 5 allows showing

that threshold voltage also depends on oxide thickness.

3.2. Influence of channel length (L_{ch}) variation on I_D current and threshold voltage

Simulation results allowing to investigate the effects of channel length on I_{DS} current are presented in figures 6 and 7.

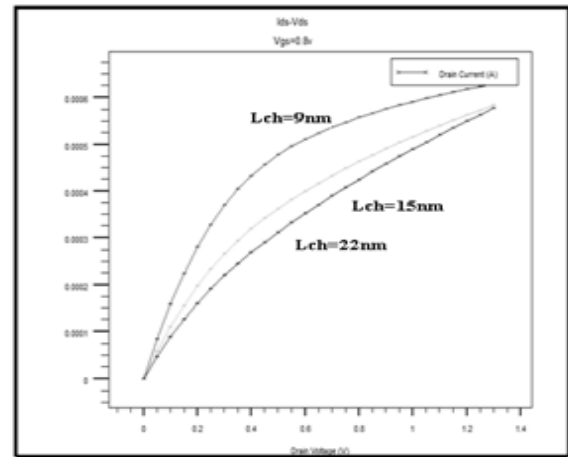


Figure.6 Output characteristics for a dual metal gate GAA MOSFETs at different channel length ($L_{ch}=9\text{nm}$, 15nm , 22nm).

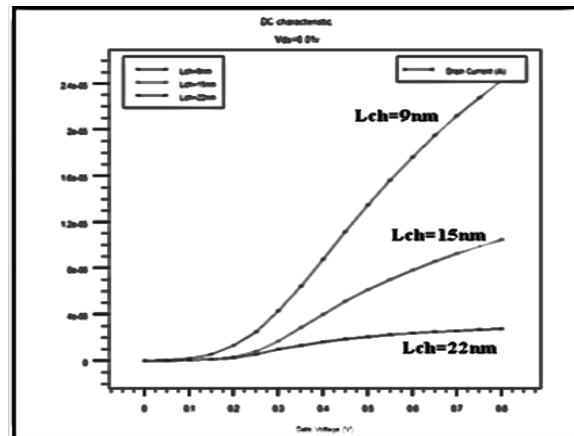


Figure7. Transfer characteristics for a dual metal gate GAA MOSFETs at different channel length ($L_{ch}=9\text{nm}$, 15nm , 22nm).

As shown in Figure 6, the drain I_{DS} is inversely related to the channel length. Thereby, when L_{ch} increases the drain currents increases and threshold voltage decreases too.

3.3. Influence of oxide layer type on ID current and threshold voltage V_{th} .

The introduction of high-k gate oxide in 2007 was a breakthrough in microelectronics as Intel developed 45nm technology processors with hafnium based material as gate dielectric. Nowadays several high-k materials ranging from Al_2O_3 to perovskites are being vigorously investigated, in order to identify a long term promising material. In this part of our study two gate dielectric, those are HfO_2 and Si_3N_4 , are used and compared to conventional gate oxide SiO_2 .

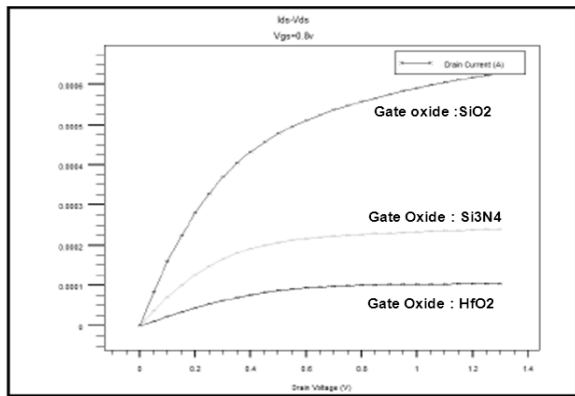


Figure..8 Output characteristics for a dual metal gate GAA MOSFETs at different High-k dielectric type (SiO_2 , Si_3N_4 and HfO_2).

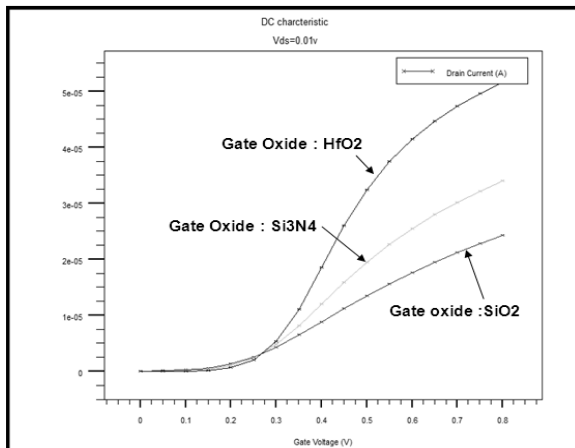


Figure. 9. Transfer characteristics for a dual metal gate GAA MOSFETs at different type of oxide (SiO_2 , Si_3N_4 and HfO_2).

Figure8 and Figure9 allow to observe the impact of gate dielectric on our device electrical characteristics. With the integration of high-k dielectrics Into GAA SOI MOSFETs, the performance of the device are supposed to be further enhanced and improved and this can be achieved using a sacrificial SiO_2 layer with a high k gate dielectric.

3.4. DIBL (Drain Induced Barrier Lowering) and Ion/Ioff ratio

The DIBL (Drain Induced Barrier Lowering) piercing said phenomenon which occurs when the dimensions of defected areas (ZCE) source / substrate and drain / substrate become comparable to the gate length. The potential distribution in the channel depends on both of the transverse field (controlled by the gate voltage), and the longitudinal field (controlled by the drain voltage) leading to drain side ZCE increasing, which causes the lowering of the barrier of source / substrate potential.

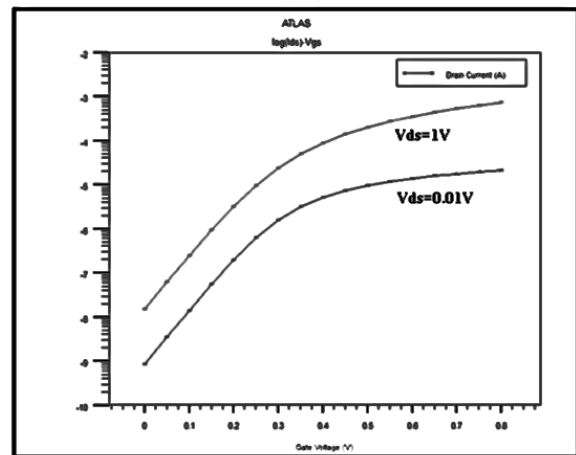


Figure.10. Highlighting of DIBL effect.

The DIBL parasitic effect appears in short channel transistors. This effect is principally due to the fact that in the weak inversion regime, there is a potential barrier between the channel region and the source. The height of this barrier is a result of the balance between drift and diffusion current between source and channel regions. If a high drain voltage is applied, the barrier height decreases leading to drain current increasing. Consequently the drain current is controlled not only by the gate voltage, but also by the drain voltage. The DIBL effect is apparent when we observe the transfer curves of our transistor for

the linear and saturated cases as shown in figure 10. In fact in the case where there is no DIBL, the two curves would match in the subthreshold regime.

The DIBL effect can be measured by the lateral shift of the transfer curves in the subthreshold regime divided by the drain voltage difference of the two curves and is given in units (mV/V). It can be expressed by:

$$DIBL = \frac{\Delta V_{TH}}{\Delta V_D} (mV/V) \quad (1)$$

From the equation 1 and Figure10 our device DIBL extracted is equal to $39mV/V$.

4. Conclusion

The downward revision of bulk planar MOSFET according to the International Technology Roadmap sheet for Semiconductors ITRS requires new structures such as MOSFETs gate all around (GAA MOSFETs). These structures can reduce short channel effects that appear below 10nm node. The structure studied in this paper is a Dual Metal Square surrounding Gate MOSFET. It has been found that the GAA MOSFETs have very good SCE immunity and are suitable to be used for low voltage low power applications. Based on the simulation results we have obtained using SILVACO software, appropriate parameters can be chosen to optimize our structure.

References

- [1] The International Technology Roadmap for Semiconductors (ITRS), 2012.
- [2] S. D. Suk, S.-Y. Lee, S.-M. Kim, E.-J. Yoon, M.-S. Kim, M. Li, C. W. Oh, K. H. Yeo, S. H. Kim, D.-S. Shin, K.-H. Lee, H. S. Park, J. N. Han, C. J. Park, J.-B. Park, D.-W. Kim, D. Park, and B.-I. Ryu, "High performance 5 nm radius twin silicon nanowire MOSFET (TSN).
- [3] J.-T. Park et al., *IEEE Trans. Elec. Dev.*, 49(12), p.22
- [4] Martinez , A. Brown, S. Roy, and A. Asenov , " Negf simulations of a junctionless if gate -all-around nanowire transistor with discrete dopants, "in *Ultimate Integration on Silicon (ULIS)2011 12th International Conference on*, P. 1-4 , IEEE , 2011.
- [5] P. Razavi , G. Fagas , I. Ferain , N. Akhavan , R. Yu, and J. Colinge , "Performance investigation of junctionless Multigate short -channel transistors , "in *Ultimate Integration on Silicon (ULIS)* , 201112th International Conference on, P. 1-3 , IEEE , 2011.WFET): Fabrication on bulk Si wafer, characteristics, and reliability," *IEDM Tech. Dig.*, 2005, pp. 717720.
- [6] H. A. El Hamid, B. Iniguez, and J. Roig, "Analytical model of the threshold voltage and subthreshold swing of undoped cylindrical gate-all-around-based MOSFETs," *IEEE Trans. Electron Devices*, vol. 54, no. 3, pp. 572-579, Mar. 2007.
- [7] G. Iannaccone, G. Curatola, G. Fiori, "Effective Bohm Quantum Potential for device simulators based on drift diffusion and energy transport ", *Simulation of Semiconductor Processes and Devices 2004*, vol. 2004, pp. 275 -278, Sept. 2004.
- [8] Ahlam Guen, B.Bouazza, C Sayah, F.Z Rahou, N.E.Chaabane Sari. Numerical Simulation of Nanoscale SOI n-MOSFETs Using SILVACO software, *International Journal of Science and Advanced Technology* (ISSN 2221-8386) Volume 1 No 10 December 2011.
- [9] Ahlam Guen, Benyoumes.Bouazza, Numerical Simulation of a Nanoscale DG N-MOSFET Using SILVACO Software, *International Journal of Science and Advanced Technology* (ISSN 2221-8386) Volume 2 No 06 June 2012 .
- [10] SILVACO, ATLAS User's Manual, Ver. 4.0, June 1995

Influence of the edge effects on the MESFET transistor characteristics

Saida Mellal, Cherifa Azizi, Mourad Zaabat and Toufik Ziar

*Faculty of exact sciences and natural and life sciences
Active Devices and Materials Laboratory*

Larbi Ben M'Hidi university, Oum El Bouaghi -Algéria-

saida_mellal@yahoo.fr

The Received date: May 25, 2014; revised date: December 10, 2014; accepted date: December 21, 2014

Abstract

A two-dimensional numerical analysis is presented to investigate the field effect transistor characteristics, Our main aim in these sheet related on the one hand to the optimization of a two dimensional (2D) analytical model for the static characteristics of short gate-length GaAs MESFET's, this model takes into account the different physical specific phenomena of the device, and on the other hand to study the influence of the effect edge on the variation of some intrinsic elements (transconductance and drain conductance). The model suggested has enables to us to calculate and trace the different series from curves. The results obtained are well represented and interpreted.

Key words: MESFET, Two-dimensional modeling, Edge effects, Characteristics (I-V, Gm, Gd)

1. Introduction

With current technological progress, the submicron components are then more powerful, but the complexity of their function increases as soon as dimensions are reduced. The development or the improvement of new dies of components requires means for the modelling, the realisation and the characterisation. It is thus very significant to predetermine the characteristic of the component, physical-modelling finds here one of its principal application.

Taking into account the complexity of the operation of a field-effect transistor to submicron gate, the designer of the components must know the influence of the technological parameters, so that this one can envisage their influence on the behaviour of the device. So in this paper the edge effects have been taken into account and their influence on the current voltage characteristics, the transconductance and drain conductance are investigate.

In this work we have made two-dimensional simulation of component with field effect's considering the effects of edge and the parasitic resistances of source and of drain, of our structure.

2. Model and voltage-current (I-V) equations

In the submicron MESFET, the channel potential cannot be entirely controlled by the gate bias and will be shifted by the penetration of lateral electric field. Therefore

the lateral field distribution at the gate edges plays an important role for the short channel effects.

Thus solution for 2D Poisson's equation satisfying suitable boundary conditions is required to model the short channel effect. A simplified self aligned GaAs MESFET is shown in Fig.1 [1], over which Poisson's equation is solved for the potential distribution $V_c(x,y)$, where 'L' is the gate length. 'a' is the thickness of the active layer.

In order to avoid the problems resulting from different surface boundary conditions, the n-GaAs layer is assumed to contact directly to the gate metal, and the absorption of electric field by the depletion charges near the source/drain is not taken into account.

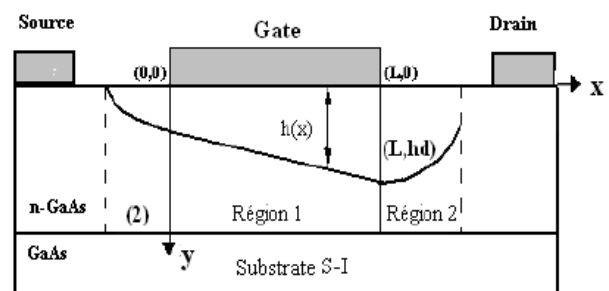


Fig. 1. Schematic diagram of a self-aligned GaAs MESFET

2.1. Calculation of the potential in the channel and the electrical field

The 2D Poisson equation for the depletion region, assuming complete depletion, is

$$\nabla^2 V_c(x, y) = \frac{d^2 V_c}{dx^2} + \frac{d^2 V_c}{dy^2} = -\frac{q}{\epsilon} N_d(y) \quad (1)$$

$V_c(x, y)$ is the electrostatic potential, q is electron charge, ϵ is the dielectric permittivity of GaAs semiconductor, $N_d(y)$ is the doping concentration, The doping is considered to be uniform, with the doping concentration N_d .

According to the superposition technique [2], (1) can be resolved as

$$V_c(x, y) = V(x, y) + V_l(x, y) \quad (2)$$

Where $V(x, y)$ is the solution of Poisson's equation (3) for the MESFET structure in one dimension along y-axis near the mid of the channel (region 1). It is this potential profile that would result if the device were completely unaffected by lateral electric fields from the source and the drain; $V_l(x, y)$ is the 2D potential function responsible for the short channel effects [6], it represents the voltage brought by the overflow of the depletion region at the drain and source sides (region2):

$$\frac{d^2 V(x, y)}{dy^2} = -\frac{q}{\epsilon} N_d(y) \quad (3)$$

$$\frac{d^2 V_l}{dx^2} + \frac{d^2 V_l}{dy^2} = 0 \quad (4)$$

To find solution of these equations (3) and (4), we used the boundary conditions expressed as [3]:

$$V(x, y)|_{y=0} = Vg - Vbi \quad (5)$$

$$\left. \frac{dV(x, y)}{dy} \right|_{y=a} = 0 \quad (6)$$

$$V_c(L, y) = V_{bi} + V_d, \quad V_l(L, y) = V_{bi} + V_d - V(y) \quad (7)$$

$$\frac{dV_c(x, a)}{dy} = 0, \quad \frac{dV_l(x, a)}{dy} = 0, \quad \frac{dV_c(L, a)}{dx} = E_s \quad (8)$$

Where V_{bi} is the potential of built-in schottky-barrier, V_g is the applied gate-source voltage, V_d is the applied drain-source voltage and E_s is the saturation electric field.

Using (5) and (6) in (3), the solution of 1D Poisson's equation is based on the fact that the depletion layer thickness under the gate, $h(x)$ is a slowly varying function in the channel.

The channel potential is obtained by integration limits with $y = h(x)$

$$V(x, y) = \frac{q}{\epsilon} \int_0^{h(x)} y N_d(y) dy + Vg - Vbi \quad (9)$$

So :

$$V(x) = \frac{qN_d}{2\epsilon} h^2(x) + Vg - Vbi \quad (10)$$

$$h(x) = \sqrt{\frac{2\epsilon(V(x) + V_{bi} - V_g)}{qN_d}} \quad (11-1)$$

Where $V(x)$ is the potential of the neutral channel with $V(0) = 0$ at the source-end and $V(L) = V_d$ at the drain-end. So that the depletion widths at the source and drain ends given respectively by :

$$h_s = \sqrt{\frac{2\epsilon(V_{bi} - V_g)}{qN_d}} \quad (11-2)$$

$$h_d = \sqrt{\frac{2\epsilon(V_d + V_{bi} - V_g)}{qN_d}} \quad (11-3)$$

To determine the two-dimensional term $V_l(x, y)$ in the frame of boundary condition Eqns (4,7,8), the solution suggested in this study may be written in the following form[1,6].

$$V_l(x, y) = \alpha [Sinh(k(L-x)) + Sinh(kx)] Sin(ky) \quad (12)$$

Where: $k = \frac{\pi}{2a}$

$$\alpha = \frac{2aE_s}{\pi(\cosh(kL) - 1)}$$

And the voltage constant:

Following (2), (10) and (12) the expression for the two dimensional potential of the channel under the gate with edge effects, is given as follows:

$$V_c(x, y) = \frac{qN_d}{2\epsilon} h^2(x) + Vg - Vbi + V_l(x, y) \quad (13)$$

2.2. Current-voltage characteristics I - V

In order to calculate the drain current expression as a function of the drain voltage for different values of the gate voltage, we use the following hypothesis:

- We neglect the current in the Y axis; this approximation is valid for the short gate components.
- The channel is divided in two regions according to the value of the electric field.
- The analytical expression of the variations of the electron mobility with electric field [4] is given by:

- For the low electric fields: $E < E_0$

$$\mu = \mu_0 \quad (14-1)$$

- For the electric fields higher than E_0 : ($E \geq E_0$)

$$\mu = \frac{\mu_0}{\left[1 + \left(\frac{E - E_0}{E_s} \right)^2 \right]^{1/2}} \quad (14-2)$$

where: E is the electric field, μ_0 is the low mobility, and E_0 is a critical field ($E_0 = 3, 5$ kV/cm for the GaAs [4]) .

The density of the current is given by:

$$j_x = \sigma(x, y, z) \cdot E_x \quad (15)$$

$$j_x = q\mu N_d \cdot E_x = -q\mu N_d \cdot \frac{dV_c(x, y)}{dx} \quad (16)$$

The drain current I_d counted positively in the sense drain source is obtained by integrating J_x across the conductor section of the channel:

$$I_d = -\int_0^z \int_{h(x)}^a j_x d_y d_z = -z \int_{h(x)}^a j_x d_y \quad (17)$$

Using single integrals, the current expression is obtained by relation:

$$I_d = \frac{(qN_d)^2 Z\mu}{\varepsilon L} \left[\frac{a}{2} (W_d^2 - W_s^2) - \frac{1}{3} (W_d^3 - W_s^3) \right] \quad (18)$$

W_s and W_d are the two dimensional widths of the depletion layer side source and drain respectively. They are calculate bay considering firstly the one-dimensional approximation $h(x)$ then we have added the **corrective term** $V_i(x, h(x))$ which results with the two dimensional analysis (equation 12) [3].

So that equations (11-1, 11-2, 11-3) becomes as follows:

$$W(x) = \sqrt{\frac{2\varepsilon(V(x) + V_{bi} - V_g - V_i(x, h(x)))}{qN_d}} \quad (19-1)$$

$$W_s = \sqrt{\frac{2\varepsilon(V_{bi} - V_g - V_i(0, h_s))}{qN_d}} \quad (19-2)$$

$$W_d = \sqrt{\frac{2\varepsilon(V_d + V_{bi} - V_g - V_i(L, h_d))}{qN_d}} \quad (19-3)$$

By deferring two expressions (19-2) and (19-3) in equation (18) the general equation of current becomes:

Linear regime

This regime exists as the electric field in the channel is low and the electron mobility is equal to μ_0 . Expression of the drain current in this regime can be written as:

$$I_d(V_d, V_g) = I_p \left[\frac{V_d - (V_i(L, h_d) + V_i(0, h_s))}{V_p} - \frac{2}{3} \left(\frac{V_d + V_{bi} - V_g - V_i(L, h_d)}{V_p} \right)^{3/2} + \frac{2}{3} \left(\frac{V_{bi} - V_g - V_i(0, h_s)}{V_p} \right)^{3/2} \right] \quad (20)$$

$$\text{Where: } I_p = \frac{(qN_d)^2 Z\mu_0 a^3}{2\varepsilon L} \quad \text{and: } V_p = \frac{qN_d}{2\varepsilon} a^2$$

Saturation regime

Drain voltage increases when the electric field in the channel increases beyond E_c . The electron mobility is given by (14-2).

The saturation value V_{dsat} is taken as the voltage where the conduction channel depleted near the drain. So:

$$V_{dsat} = V_p + V_g - V_{bi} + V_i(L, h_d) \quad (21)$$

The simplified expression for the saturation drain current is:

$$I_{dsat} = I_p \left[\frac{1}{3} - \left(\frac{V_{bi} - V_g - V_i(0, h_s)}{V_p} \right) + \frac{2}{3} \left(\frac{V_{bi} - V_g - V_i(0, h_s)}{V_p} \right)^{3/2} \right] \quad (22)$$

$$\text{With: } I_p = \frac{(qN_d)^2 Z\mu a^3}{2\varepsilon L}$$

3. Transconductance and drain conductance

The expression of I_d is used to calculate the two basic parameters of the transistor, which are the transconductance g_m and the channel conductance g_d more commonly known as drain conductance.

- The transconductance is the expression of the control mechanism of a transistor: it represents the variation of the current in the channel modulated by the gate voltage at constant drain-source voltage [5].

In the Linear regime

$$g_m = \frac{Z\mu_0}{L} (2\varepsilon q N_d)^{1/2} \left[\frac{(V_d + V_{bi} - V_g - V_i(L, h_d))^{1/2}}{V_p} - \frac{(V_{bi} - V_g - V_i(0, h_s))^{1/2}}{V_p} \right] \quad (23)$$

In the saturation regime

$$g_{msat} = \frac{Z\mu}{L} (2\varepsilon q N_d)^{1/2} \left[\left(\frac{V_p}{V_p} \right)^{1/2} - \left(\frac{V_{bi} - V_g - V_i(0, h_s)}{V_p} \right)^{1/2} \right] \quad (24)$$

- The conductance reflects the resistance of the channel: it is the variation of the drain current according to the V_d voltage variation, with constant polarization of the gate.

In the Linear regime

$$g_d = \frac{Z\mu_0}{L} (2\varepsilon q N_d)^{1/2} \left[\left(\frac{V_p}{V_p} \right)^{1/2} - \left(\frac{V_d + V_{bi} - V_g - V_i(L, h_d)}{V_p} \right)^{1/2} \right] \quad (25)$$

In the saturation regime

The conductance is perfectly zero,

$$g_{dsat} = 0 \quad (26)$$

4. Influence of parasitic resistances

The characteristics that we have presented are those of the internal or intrinsic sizes (L_c, V_s, V_d). to obtain the external or extrinsic characteristics of the component (L_e, V_{ds}, V_{gs}), it is enough to take into account the effect of parasitic resistances to access of source R_s and drain R_d , and also the effect of R_p parallel resistance to the canal on the values of polarization voltages [4] as shown in figure 2.

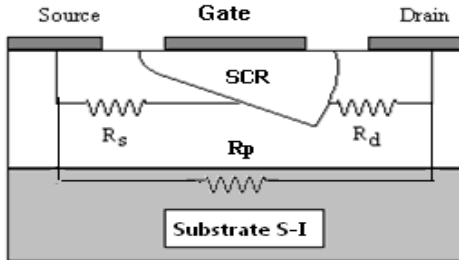


Figure 2 : Parasitic resistances in the MESFET GaAs.

To obtain the real expressions of characteristics I_d, g_m and g_o , it is enough to replace the intrinsic terms by the extrinsic terms in all the preceding relations:

$$\begin{aligned}
 I_d &= I_{ds} - (V_{ds} / R_p) \\
 V_d &= V_{ds} - (R_s + R_d) I_d \\
 V_g &= V_{gs} - R_s I_d
 \end{aligned}
 \tag{27}$$

5. Results and discussions

Software of simulation based on the expressions established in the preceding paragraphs is realized in **Matlab**. The study was carried out on a submicron gate GaAs MESFET transistor which parameters gathered in the table (1).

L (μm)	a(μm)	Z(μm)	μo(m²/Vcm)
1	0,153	100	0,2800
Nd(At/m³)	Vs(m/s)	Vbi(V)	Vp(V)
1,17 10 ²³	3,6 10 ⁵	0,85	1,93

Table (1): GaAs MESFET transistor parameters

Figures (3) and (4) shows the variation of the potential $V(x,y)$, which result on the two dimensional analysis (Eqn12). Where the voltages $V_i(0,hs)$ and $V_i(L,hd)$ are plotted as a function of drain and gate bias .

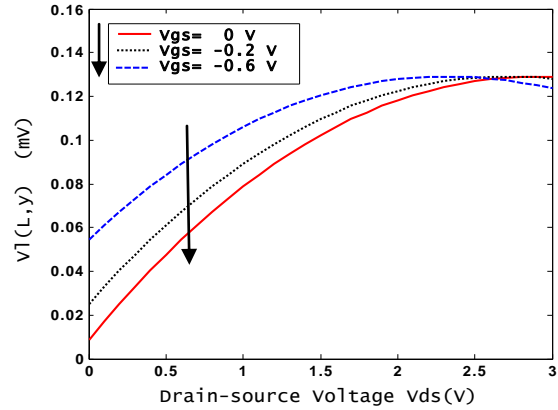


Figure 3: Variations $V_i(L,hd)$ voltages according to drain bias

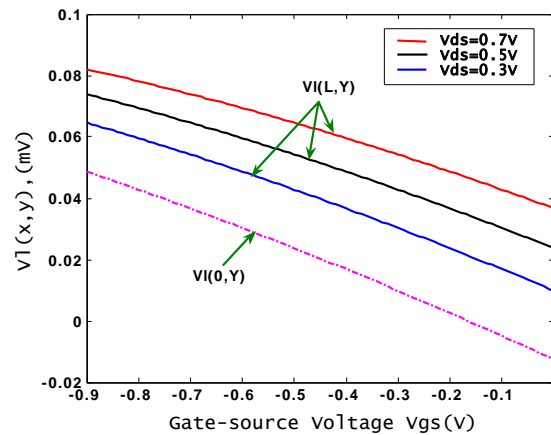


Figure 4: Variations $V_i(0,hs)$ and $V_i(L,hd)$ voltages according to gate bias

In these figures, we noticed that the voltages $V_i(0,hs)$ and $V_i(L,hd)$ of the edge effects are found to be positive and both these quantities increases gradually as the absolute value of the gate voltage " V_{gs} " increases, and also with the increase of the voltage drain " V_{ds} ".

For a long channel device, V_g completely control depleting the semiconductor channel. However in short channel devices, part of channel depletion is under the control of source and drain bias. As the channel length shortens, the close proximity of the source and drain region occurs the fraction of the depletion charge in the channel. In other words, both the gate and source-drain voltages share control of the charge density below the gate. This effect is described by the figures (5), (6) and (7) were effects of $V_i(0,hs)$ and $V_i(L,hd)$ voltages on the drain current, transconductance and drain conductance of the GaAs MESFET are plotted with and without edge effects.

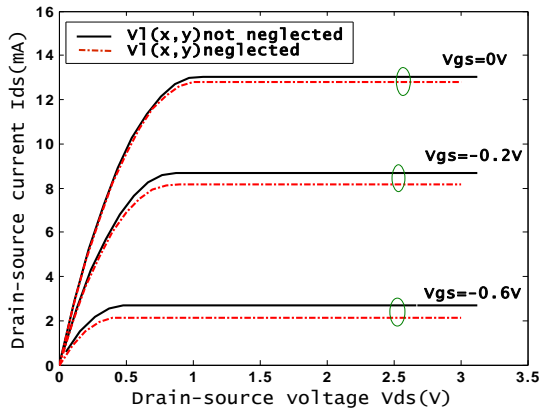


Figure 5: Variations I-V characteristics of the MESFET transistor

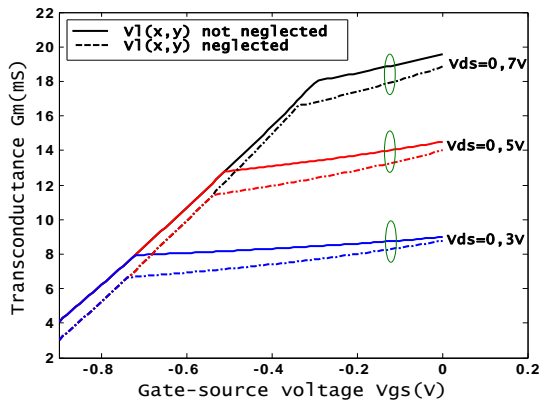


Figure 6 : Variation of the transconductance according to the gate voltage for the MESFET

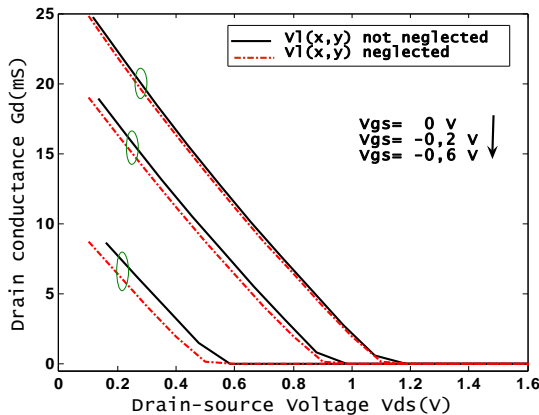


Figure 7: Variation of the conductance according to the drain voltage for the MESFET

Figure (5) shows a comparison between the drain current characteristics with and without edge effects. From the figure it is clear seen that edge effects $V_l(x,y)$ promotes the passage of more drain current. This is mainly due to the depletion region from the source and drain which are overlapped with the channel charge. In long channel devices, this part is negligible comparing with the area of effective device channel. However, in short channel device,

this overlapped part cannot be neglected anymore and the previous approximation does not work. With the consideration of overlapped parts, the shape of the depletion charge cross-section can be described as shown in figure (1) and drain current can be calculated as expressions (20) et (22).

Such a functional dependence of the drain current suggests more involved relations for the drain conductance g_d and the transconductance g_m of the device. Like drain current, both g_d and g_m are also functions of edge effects. Figures (6) and (7) shows the changes in the values of drain conductance and transconductance caused by the voltages $V_l(0,hs)$ and $V_l(L,hd)$, that are relatively sharper with the increase of V_g and V_d

6. Conclusion

After we solved analytically the two-dimensional Poisson equation, we have presented the influence of edge effects for I-V characteristic, transconductance and drain conductance of the MESFET. When the depletion region extends at the drain side and source side, the depletion width is also affected by the edge effects. This has a direct influence on the characteristics of the transistor.

The simulation results are well presented and discussed, the corrective term $V_l(x,y)$ gives a real approximation for the potential distributions and depletion-layer form, that are used for the calculation of the short canal device characteristics .

References

- [1] S.Khemissi, C Kenzai and all, "Influence of physical and geometrical parameters on electrical properties of short gate GaAs MESFET's", SPQEO Vol 9 N°2, pp 34- 39, 2006.
- [2] K.N. Ratnakumar, J.D. Meindel, "Short-channel MOST threshold voltage model," IEEE J. Solid State Circuits 17 (1982) 937-947.
- [3] S.Khemissi, C. Azizi "A two-dimensional model for the potential distribution and depletion layer width of the short gate-length GaAs MESFET's", 2010 XIth International workshop on symbolic and numerical methods, modeling and applications to circuit design (SM2ACD).
- [4] M. S. Benbouza and N.Merabtine," impact of gate length on equivalent circuit elements in GaAs MESFET transistors", Journal of Electron Devices, Vol. 18, 2013, pp. 1590-1594
- [5] Sneha Kabra and all ." Two-dimensional subthreshold analysis of sub-micron GaN MESFET" Microelectronics Journal Vol 38, pp 547-555, May 2007.
- [6] Shweta Tripathi, S. jit " A two-dimensional (2d) potential distribution model for the short gate-length ion-implanted GaAs MESFETs under dark and illuminated conditions " J. Nano- Electron. Phys 3 (2011) No1, P. 868-877

Numerical simulation of distribution of soot size in a laminar flame

D. Lalmi^a and R. Hadeb^b

^aFaculty of exact sciences, natural sciences and life, Larbi Ben Mhidi University, OEB Aleria

^bFaculty of sciences and applied sciences, Larbi Ben Mhidi University OEB Aleria

Eldjemoui@gmail.com

Received date: May 25, 2014; revised date: December 18, 2014; accepted date: December 21, 2014

Abstract

The objective of this study is to determine the characteristics of soot (size and distribution) in a laminar flame of diffusion (ethylene-air). The non-intrusive technique used is the incandescence induced by laser (LII) discovered by Melton [1].

The interaction laser-particle of soot is described by an ideal model of heat transfer and mass including the various modes of thermal losses (vaporization, conduction, radiation). The equations obtained describing the temporal evolution of the diameter and the temperature of the particle are solved numerically. The ideal model is validated by experimental measurements and confrontation with various powers of the exciting laser, the result is satisfactory.

Key words: Incandescence Induced by Laser, Flame, Soot, Transfer of heat and mass.

1. Introduction

Laser-induced incandescence (LII) phenomenon is known since 1970 its principle is simple: under the effect of a radiation laser (typically an impulse of 10ns), the particles of soot present in a flame heat up very quickly (temperature can border 4000K), then cool by various thermal processes of transfer (vaporization, conduction and radiation) schematized in Fig.1, which the radiation of that transfer one names incandescence.

Thus the expressions of the energy balance on the level of the soot particle are gathered by Melton [1] in one only. It can be written in the form:

$$Q_{Int} = Q_{abs} - (Q_{sub} + Q_{con} + Q_{rad}) \quad (1)$$

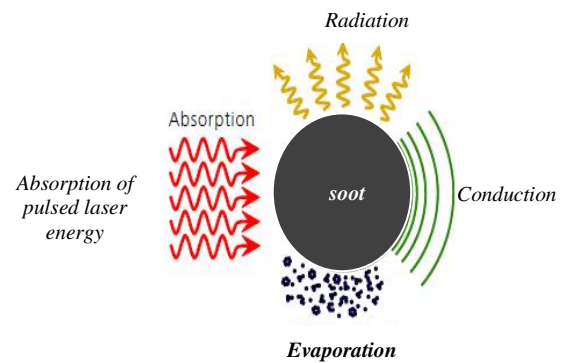


Fig.1. Modelling of LII

This equation coupled to that of conservation of the mass makes it possible to calculate, using a numerical routine, the soot temperature and diameter in all along LII process. An illustration of the evolution of the relative energy values during this process under conditions of atmospheric pressure is reproduced on Fig.2.

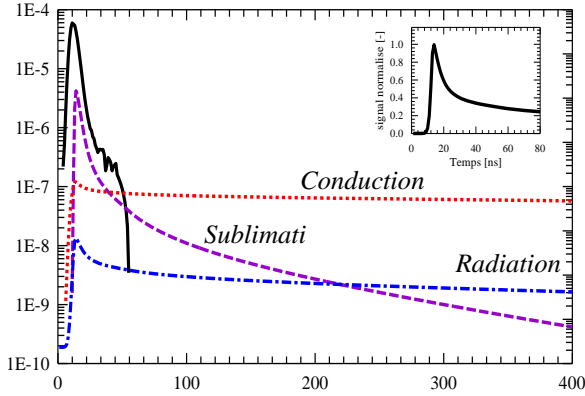


Fig.2. Evolution of the various energy terms in time ($F=0.227\text{J}/\text{cm}^2$, $T_0=1900\text{K}$, $D_0=35\text{nm}$)

One can observe that in the case of strong laser flows, sublimation is the energy process dominating during the first part of the cooling of the particle, the second phase roughly beginning 100 NS after (in condition of atmospheric pressure) is dominated by the conduction of heat transfer .

In addition, Melton [1] indicates the value of 3915 K as the temperature from which vaporization deviate dominantly. The thermal radiation is the least intense energy process during cooling of the particles. In the same figure, also the instantaneous evolution of signal LII is represented.

2. Intensity of the signal of induced incandescence

LII Signal resulting from a soot particle is collected with the wavelength λ which is expressed using the law of Planck corrected by a term of emissivity $\varepsilon(\lambda)$:

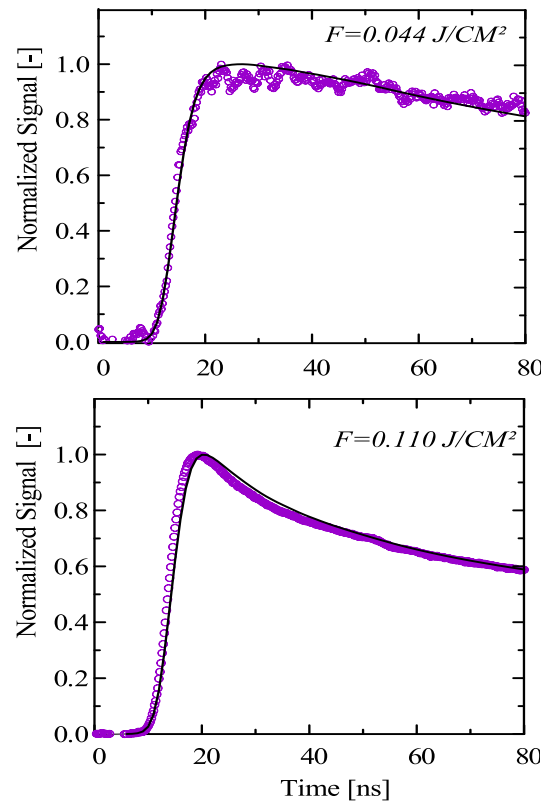
$$S_{LII}(t) = C \frac{2\pi c^2 h}{\lambda_{det}^5} \left(\exp\left(\frac{hc}{\lambda_{det} k_B T(t)}\right) - 1 \right)^{-1} \pi^2 D^3(t) \frac{E_m}{\lambda_{det}}$$

Where C is a constant related to the device of detection, h , C , K_B are respectively the Planck's constant, the speed of the light and the Boltzmann constant, and $T(t)$ is the soot temperature at the moment after the beginning of the laser impulse [4]. Of the incandescence resulting ones from a volume of measurement containing N_p particles of soot is thus

proportional to $N_p D^3$ (that is to say the volume fraction fv) this is why the quantitative results on soot relate to in priority this size [3].

3. Results

The validation of the our ideal model is made with real measurements [2]. In the latter, the temporal intensity of signal III was measured on a vast range of power of the going laser of $F=0.044\text{J}/\text{cm}^2$ until $F=0.830\text{J}/\text{cm}^2$. The atmospheric flame is of diffusion type where the fuel C_2H_2 jet is surrounded by a flow of air. The soot particles were heated with impulses of a laser wavelength of excitation $\lambda_{exc} = 532\text{ nm}$. The initial diameter of the soot particle is $D_0 = 35\text{ nm}$ and the temperature of gases is estimated at 1900 K . Fig.3 shows a comparison between the results of the ideal model and experimental measurements for various powers of the laser F .The model qualitatively shows a good agreement with measurements: a fast growth followed by a slow fall to low values of F, an increase and a faster decrease for the great values of the density F.



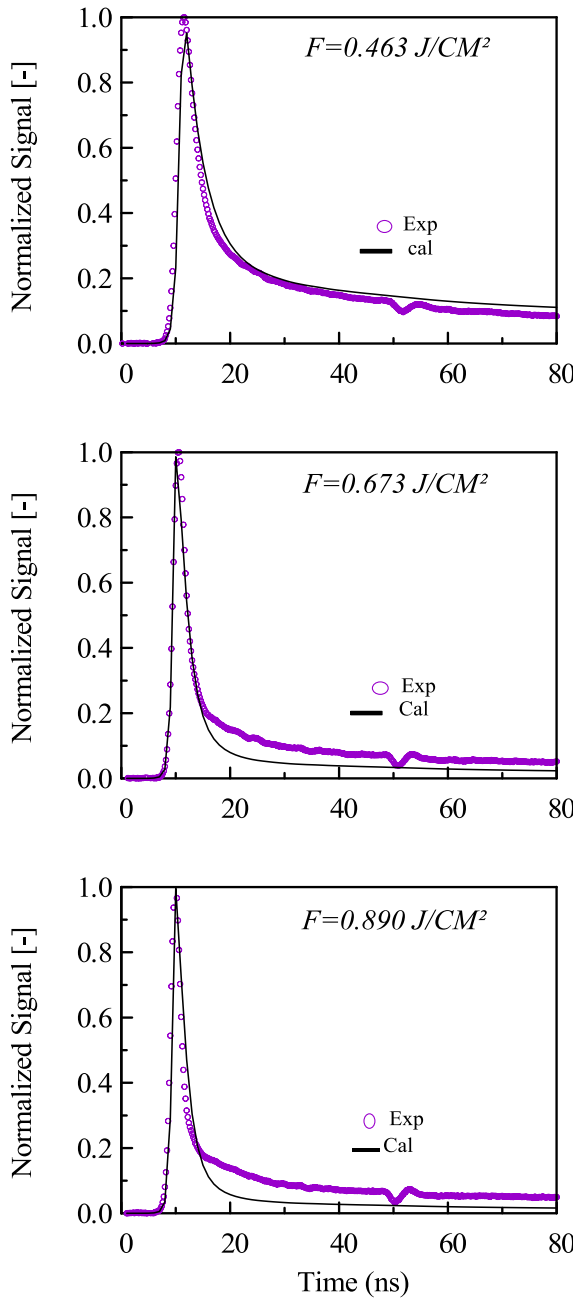


Fig.3. LII Model Validation

Then, this ideal model is extended to a whole of particles defined by a polydispers distribution of size of the lognormal type with a mean diameter D_m and a standard deviation σ_g .

The determination of the both $(DM \sigma_g)$ in each fire point is obtained by the best fitting signal measured S_{II}^{mes} and a theoretical signal $S_{II}(t, DM \sigma_g)$ [5]. An example is presented in (Fig.4).

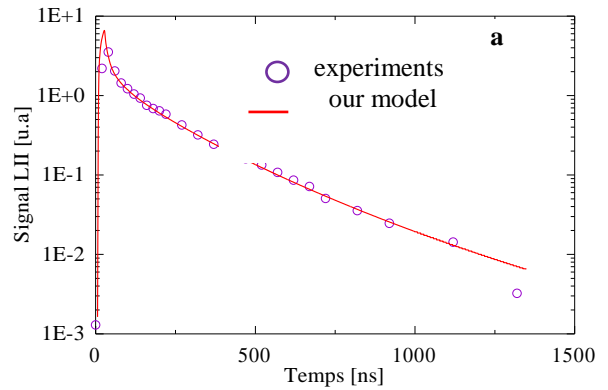


Fig.4.a- Temporal evolution of signal LII (HAB=30mm, r=3mm, $D_m=28nm$, $\sigma_g=0.34$)

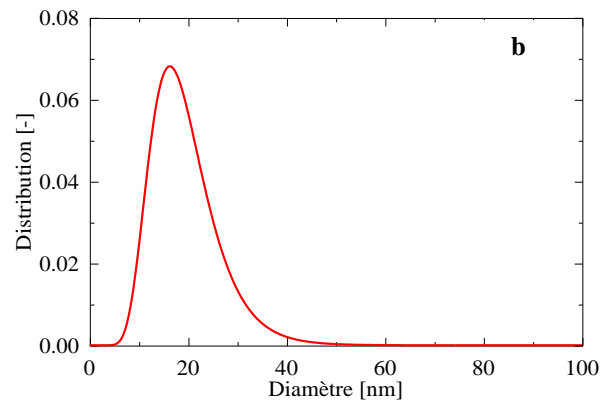


Fig.4.b-Granulometric distribution of soot (HAB=30mm, r=3mm, $D_m=28nm$, $\sigma_g=0.34$)

We also simulated with not detail flame studied to obtain qualitative results on the species generated during combustion. The mechanism of reaction GRIMECH 2 (49species, 279 reactions) was used in the commercial code Fluent 2D-Axisymmetric[6].

The adopted geometry is shown in Fig. 4 with the conditions necessary limits.

The gas is inject at 300K with axial velocity profiles only governed by the volume flow:

$$0 \leq r \leq R_0 \quad U(r) = \frac{2Q_f}{\pi R_0^2} (1 - r/R_0)$$

Where $Y_{C_2H_4} = 1$ et $Y_{i \neq C_2H_4} = 0$

And: $Y_{N_2} = 0.767$; $Y_{O_2} = 0.233$

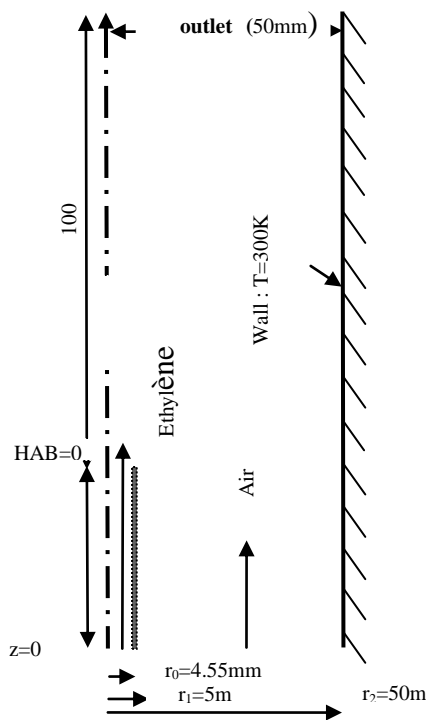


Fig.5.Geometric Configuration

It is noted that for the simulation of the diffusion flame in which the air and fuel are not premixed comprises a spreading zone reactions. In the pyrolysis zone (Hab = 10 mm) large hydrocarbons molecule of the fuel, brought to high temperature, decompose into fragments, some of which combine reactions carbonaceous rings or acetylene (C₂H₂) and carbon radicals play a key role. In the forming zone of the soot (Hab = 10 to 20 mm), these molecules are polymerized to form the soot particles precursor, liquid and almost transparent. With the collision phenomena, these precursors grow in the growth zone (Hab = 30 to 40 mm) lose a part of their hydrogen and form aggregates of solid particles absorbing the light.

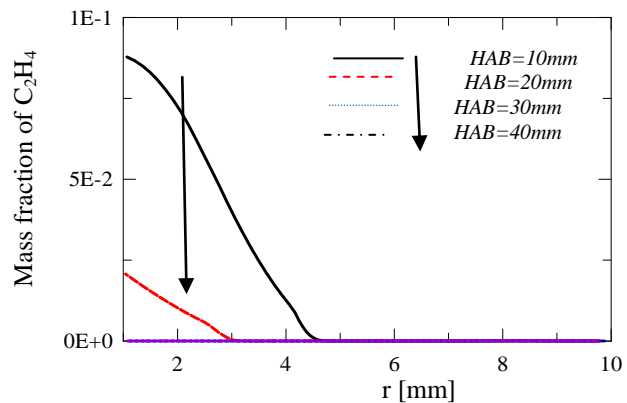


Fig.6. Radial evolution of mass fraction of C₂H₄

In Fig.6 we present the radial evolution of mass fraction from some species for different height above burner (HAB).

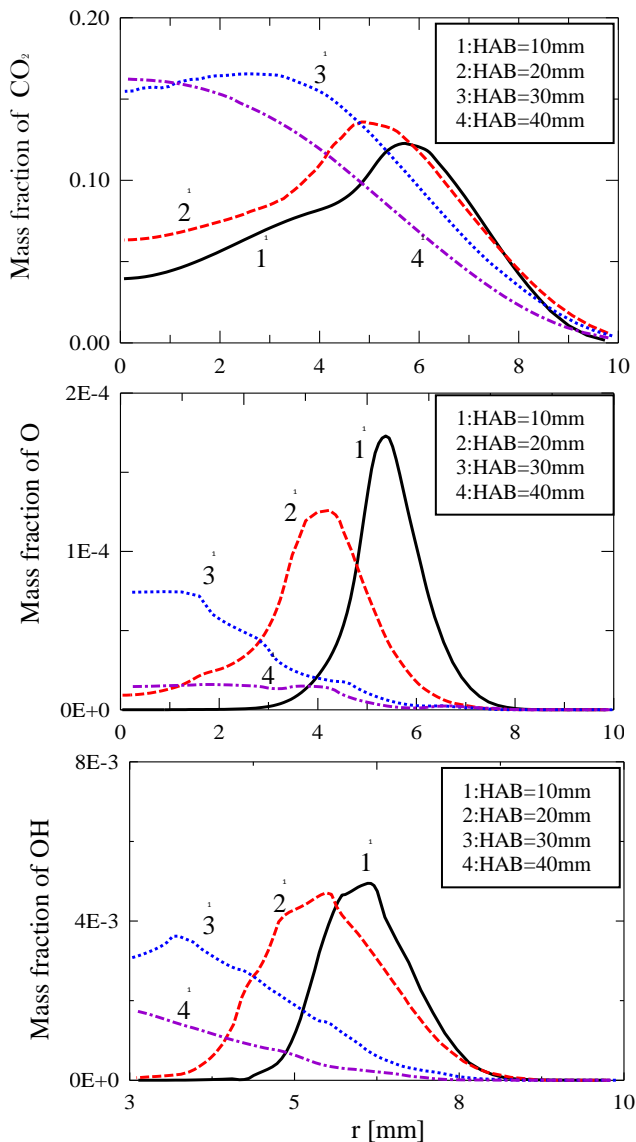


Fig.7. Radial evolution of mass fraction of CO_2 , OH, and O

This work has been devoted to the application of the LII technique for determining the size of the soot particles in a laminar diffusion flame.

This non-intrusive technology based on an analysis of the radiation emitted by the particles heated with the laser flux to determine the size and concentration of the soot. Among the various modes of energy exchange in charge of the heating and cooling of the

soot particles or the LII process a theoretical model able to predict the temporal evolution of the LII signal having been set up to estimate the mean particle diameter of soot was developed for conditions in free molecular regime and confirm with measures that confrontation is satisfactory. we proved that the LII signal is proportional relationship with the concentration of soot and the characteristic time of the decay is dependent on the men size of primary particles; plus a large particle is more it cools slowly. finally completed this work by a single flame numerical simulation considered.

References

- [1]Melton L.A., Soot diagnostics based on laser heating, *Appl. Opt.* 23 (1984), 2201-2208.
- [2]Michelsen H.A., Understanding and predicting the temporal response of laser-induced incandescence from carbonaceous particles, *J. Chem. Phys.*118 (2003), 7012-7045.
- [3]Hadeif R., Krüger V., Geigle K.P., Tsurikov M.S., Schneider-Kühnle Y., Aigner M., Measurements of soot size and concentration in the laminar premixed flame, *Oil & Gas Science and Technology - Rev. IFP* 61 (2006), 691-703.
- [4]Michelsen H.A., Liu F., Kock F., Bladh H., Boiarciuc A., Charwath M., Dreier T., Hadeif R., Hofmann M., Reimann J., Will S., Bengtsson P.-E., Bockhorn H., Foucher F., Geigle K.P., Mouaïm-Rousselle C., Schulz C., Stirn R., Tribalet B., Modeling laser-induced incandescence of soot: a summary and comparison of LII models, *Appl. Phys. B*. 87 (2007), 712-745.
- [5]H. Bladh, On the Use of Laser-Induced Incandescence for Soot Diagnostics From Theoretical Aspects to Applications in Engines, Doctoral, PhD Dissertation Division of Combustion Physics Department of Physic, Lund University, ISBN 978-91-628-7142-0 .
- [6]F. Liu, K. J. Daun, D. R. Snelling, And G.J.Smallwood, Heat conduction from a spherical nano-particle: status of modeling heat conduction in laser-induced incandescence, *Appl. Phys. B* 83, 355 (2006)

Fabrication and characterization of zinc oxide (ZnO) thin films based humidity sensor with fast response by sol-gel method

Ghanem Salah, Telia Azzedine and Boukaous Chahra

*University of Constantine 1, Department of electronic,
Laboratory of Microsystems and instrumentation (LMI)
Constantine, Algeria*

Received date: May 25, 2014; revised date: December 10, 2014; accepted date: December 21, 2014

Abstract

Present work deals with deposition of Zinc oxide (ZnO) thin films by sol-gel method. Sol was prepared using zinc acetate, 2-Methoxyethanol and monoethanolamine (MEA) as starting materials. Films were grown using spin coating method and annealed at 500 C. ZnO films morphology was investigated by Scanning Electron Microscope. SEM images reveal that films are composed with wrinkles network. Crystalline structure was studied by means of X-ray diffraction analysis. XRD patterns exhibit three strong peaks (101), (002) and (100) planes assigned to Wurtzite structure. The obtained results for electrical properties were reported. Relative humidity sensing properties has been studied and determined by variation of electrical resistance measurements at various humidity levels. Our experimental results show that the temperature and morphology have strong influence on the response and recovery times of sensing.

Keywords—ZnO; sol-gel; thin films; XRD; SEM; Humidity sensing; Response and recovery time

1. Introduction

Different sensing materials have been developed including metal oxides [1] and polymers [2] to detect different gases [3], humidity [4] and temperature [5]. These sensors are used in diverse applications such as healthcare. ZnO is n-type semiconductor; it is one of the most promising materials for sensor applications due to its sensitivity and easy doping method for improving sensing performances. ZnO has been extensively studied and proved to be an excellent gas sensitive material for detection of toxic gases, such as CH₄ [6] and CO [7]. Various studies are focused on humidity sensing [1,4]. The increasing interest to use ZnO as humidity sensor is due to its special chemical property to adsorb water molecules [8] and also to the fact that can be grown in different shape and morphologies such as nanorods [9], wrinkles network [10] and nanowires [11]. ZnO thin films having these morphologies have been successfully synthesized and applied in humidity sensing [11]. Humidity monitoring is used extensively in industrial sectors and scientific applications. Researchers have developed humidity sensing architectures using different sensing techniques

including quartz crystal microbalance (QCM) [1], impedance [12] and surface acoustic wave (SAW) [13]. Electrical impedance of ZnO sensors change with humidity due to the enhancement of the adsorbed water on sensor surfaces [4]. It is well known that a powerful sensor must have narrow hysteresis [8] high sensitivity, rapid response and recovery times [14]. In present study, we prepared a humidity sensor based on ZnO thin films. The surface morphology and crystalline structure of ZnO were analyzed by SEM and XRD. Electrical properties and humidity capabilities of ZnO thin films were investigated by impedance variation technique at different temperatures and humidity levels (RH%) where the response and recovery times have been determined.

2. Experimental

2.1. Elaboration procedure

ZnO sol was prepared using zinc acetate, 2-Methoxyethanol and monoethanolamine (MEA) as the solute, solvent and stabilizer respectively. The molar ratio of MEA to zinc acetate was kept at 1.0 and

the Zn concentration was 0.5mol/L. The resulting solution was stirred by a magnetic stirrer at 70°C for one hour. The solution was aged for 24 h and then ZnO thin films were coated by spin coating method on glass substrate at 4000 rpm. After each coating, samples were dried at 280°C for 8 minutes. At the end of process, substrates were annealed at 500°C in ambient atmosphere for 2 hours. The crystalline structure was analyzed by X-ray diffraction using a XRD Bruker D8 Advance. Surface morphology of film was observed using TESCAN VEGA TS 5130 MM scanning electron microscope (SEM).

2.2. Sensing test

Sensor based on ZnO thin films was placed on a heating system (GEFRAN 1000) into an airtight chamber (fig.1). Air compressor was used to push wet air to the chamber and a vacuum pump was used to evacuate it outside. Two electrical contacts were connected through a hole fitted with a vacuum seal gasket in that chamber. System of impedance measurement was used to collect data. TESTO Worldwide hygrometer was used to measure the RH inside the chamber.

3. Results and discussions

3.1. Structural characterizations

The crystalline structure of ZnO thin films prepared was investigated by X-ray diffraction.

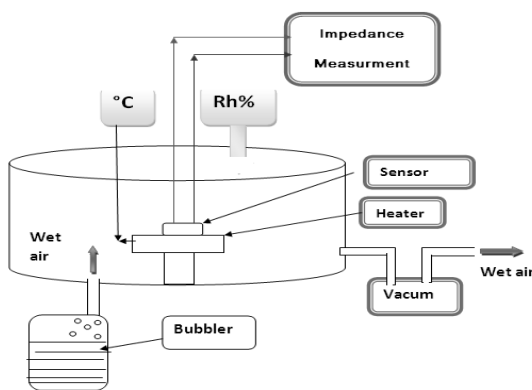


Fig. 1. Experimental setup to measure the response of sensor.

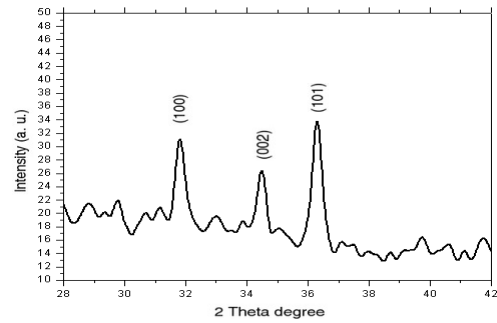


Fig. 2. XRD pattern for ZnO film prepared

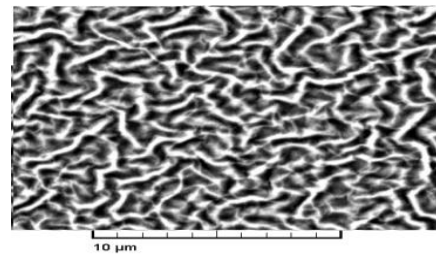


Fig. 3. SEM image of ZnO film

Figure 2 shows the recorded XRD patterns. As can be seen these patterns correspond to three diffraction peaks assigned to (100), (002) and (101) planes. The strongest one is (101), this result implies that films have a hexagonal wurtzite structure with preferred orientation along the (101) plane. Similar results have been observed by Chien-Yie Tsay et al [15] on undoped, Ga, In, and Zr doped ZnO thin films, but Sn doped ZnO thin films has randomly oriented growth behavior.

Grain size D of crystallites was found 25.62 nm; it was calculated using a well-known Scherrer's Formula [10],

$$D = \frac{0.94\lambda}{\beta \cos\theta} \quad (1)$$

Where $\lambda = 0.15406$ nm is the wavelength of X ray, β is the full width at half maximum (FWHM) of the peak and θ is the Bragg's angle.

Surface morphology of thin films has been studied by a scanning electron microscope. Figure 3 shows the plan view of SEM micrograph of annealed ZnO thin films where continuous surface with irregular fiber-like and wrinkle network structure were observed. The

morphology is homogenous with fibers of 500 nm and 2300 nm as width and length respectively. Similar morphologies have been observed in undoped [16] and doped ZnO thin films [17,18]. Wrinkle network structure and high roughness surface lead to much more area; it means that such area has more active sites for dissociation and condensation of water molecules which is interesting for humidity sensing.

3.2. Electrical proprieties

Electrical properties were characterized by mean of four probe resistivity and Hall effect measurement. The obtained results in ZnO film are:

$n=7.79 \times 10^{13} \text{ cm}^{-3}$, $\mu = 18.33 \text{ cm}^2 \text{ v}^{-1} \text{ s}^{-1}$ and $\sigma = 2.28 \times 10^{-4} (\Omega \text{ Cm})^{-1}$ for free carriers concentration, electron mobility and conductivity respectively. Zhanchang Pan et al [19] have reported that the co-doping with Al and Sn may be leading to improvement in conductivity of the ZnO thin films.

3.3. Sensing test

In order to investigate humidity sensing properties of device based on zinc oxide wrinkles network structure, we have studied resistance variation depending on relative humidity at 25°C, 50°C, 75°C and 100°C respectively. Figure 4 shows a variation of resistance according to humidity rates on adsorption process (when RH change from 15% to 95%). As we can see the corresponding resistance decreases obviously and almost linearly by enhancing humidity. The process of adsorption of water molecules due by increase of RH causes the decrement of impedance to about 0.4 MΩ in four cases. By decrement of RH level, impedance returns to initial state but not precisely in same values (not mentioned in curve). Juan Xie et al [20] reported that chemisorption occurs at relatively low RH value to form two surface hydroxyls per water molecule, when humidity rises; physisorption of water molecules takes place.

Response and recovery times corresponding to water molecules adsorption and desorption processes at RH=95% were evaluated to understand the performance of the humidity sensor and temperature effect. Figure 5 and figure 6 show relative sensitivity

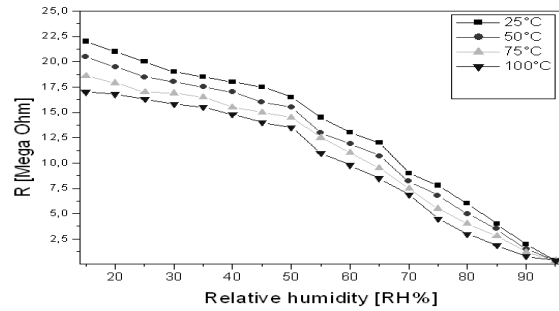


Fig. 4. Resistance variation with RH% at different temperatures.

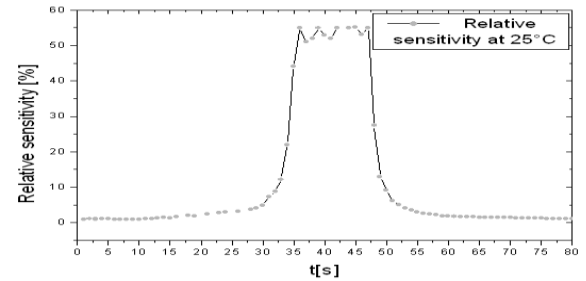


Fig. 5. Relative sensitivity of ZnO humidity sensor at 25°C.

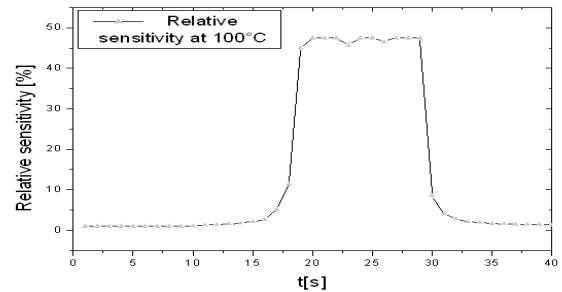


Fig. 6. Relative sensitivity of ZnO humidity sensor at 100°C

for one cycle on ZnO sensors heated at 25 and at 100°C. We defined sensitivity following this formula:

$$S = \frac{Ra}{Rh} \quad (2)$$

Ra is the resistance at RH%=15 and Rh is the resistance measured at humidity level defined. Four different values of the response and recovery times were mentioned in fig.7 at four temperatures. It is

observed that in all cases the resistance decreases to close values. The response time (as the humidity changes from 15% to 95% RH) is about 22 s and it continues to be shorter with temperature increment until seven seconds at 100°C. The recovery time (as the humidity changes from 95% to 15%) is about 30 s and it continues to be shorter with the increasing of temperature until the 14 seconds at 100°C. The recovery time is relatively slow and it generally takes more seconds to completely recover the sensor original state once wet air evacuated and this might be induced by the chemisorption on the surface of sensing element the adsorbed water might not be entirely removed. Temperature of ZnO films surface spread toward the water layers and increase the mobility of charges carriers in it therefore hopping frequency of protons is more rapid and influence on the conductivity the consequence the response is more rapid. In order to evaluate the performance of ZnO Wrinkle network humidity sensors in practice we have studied the stability behavior the sensor were exposed in air for 60 days, followed by measuring impedances at various RH levels. As shown in fig.8 there is only an inconspicuous change in the impedances, which directly confirms the potential application of ZnO sensors for humidity monitoring.

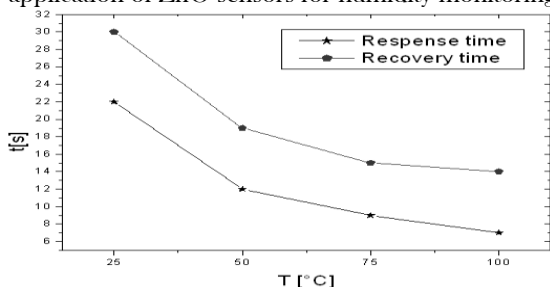


Fig. 7. Variation of response and recovery times with temperature

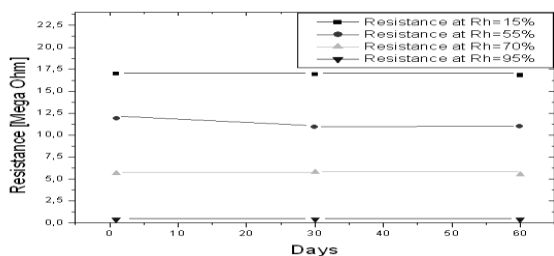


Fig. 8. Stability of the ZnO humidity sensor at various RH levels.

4. Conclusion

ZnO thin films with wrinkle network structure were elaborated by sol-gel process. Sensitivity of ZnO thin films to humidity was investigated by resistance variation, resistance of ZnO sample decrease with the increase of RH%. Shorter response time was observed when samples were heated.

References

- [1] A. Erola, S. Okurb, B. Combaa et al, *Sensors and Actuators B* 145 (2010) 174-180.
- [2] Andrii Buvailo, Yangjun Xing, Jacqueline Hines et al, *Sensors and Actuators B* 156 (2011) 444-449.
- [3] Manmeet Kaur, Namrata Jain et al, *Sensors and Actuators B* 133 (2008) 456-461.
- [4] Pranab Biswa, Souvik Kundu, P. Banerji, et al, *Sensors and Actuators B* 178 (2013) 331- 338.
- [5] Richa Srivastava, *Journal of Sensor Technology*, 2012, 2, 12
- [6] Oleg Lupan, Lee Chow, Guangyu Chai, *Sensors and Actuators B* 141 (2009) 511-517.
- [7] Ting-Jen Hsueh, Yi-Wen Chen, Shou-Jinn Chang et al, *Sensors and Actuators B* 125 (2007) 498-503.
- [8] Fu-Shou Tsai, Shui-Jinn Wan, *Sensors and Actuators B* 193 (2014) 280- 287.
- [9] D. Polsongkram P. Chamminok, S. Pukird, et al *Physica B* 403 (2008) 3713- 3717.
- [10] Chien-Yie Tsai, Kai-Shiung Fan, Yu-Wu Wang et al, *Ceramics International* 36 (2010) 1791-1795.
- [11] Sheng-Po Chang, Shou-Jinn Chang Chien et al, *Superlattices and Microstructures* 47 (2010) 772-778.
- [12] Qing Yuan, Nan Li, Jinchun Tua et al, *Sensors and Actuators B* 149 (2010) 413-419.
- [13] Hoang-Si Hong, Duy-Thach Phan, Gwi-Yang, *Sensors and Actuators B* 171- 172 (2012) 1283-1287.
- [14] Qi, Tong Zhang, Qingjiang Yu, Rui Wang et al, *Sensors and Actuators B* 133 (2008) 638-643.
- [15] Chien-Yie Tsay, Wen-Che Lee, *Current Applied Physics* 13 (2013) 60-65.
- [16] Chien-Yie Tsay, Kai-Shiung Fan, Yu-Wu Wang et al, *Ceramics International* 36 (2010) 1791-1795.
- [17] N. V. Kaneva, C. D. Dushkin *Bulgarian Chemical*, 43 (2011), 259-263.
- [18] Saliha Ilican, Mujdat Caglar, Yasemin, *Applied Surface Science* 256 (2010) 7204-7210.
- [19] Zhanchang Pan Xinlong Tian, Shoukun Wu et al, *Applied Surface Science* 265 (2013) 870- 877.
- [20] Juan Xie, Hu Wang, Yuanhua Lin, et al, *Sensors and Actuators B* 177 (2013) 1083- 108.

Structural, Optical and Electrical Properties of ZnO:Fe Thin Films Grown by Spray Pyrolysis

Nadjate Abdelmalek⁽¹⁾, Lazhar Hadjeris^(1*), Dalila Allouane⁽¹⁾, Labidi Herissi⁽¹⁾, Saâd Rahmane⁽²⁾ and Hassiba Moualkia⁽¹⁾

⁽¹⁾Laboratoire des Matériaux et Structure des Systèmes Electromécaniques et leur Fiabilité, Université Larbi Ben M'Hidi, Oum.El.Bouaghi, Algérie.

⁽²⁾Université Mohamed Lakhdar - Biskra, Algérie.
l.hadjeris@gmail.com

Received date: May 25, 2014; revised date: December 20, 2014; accepted date: December 21, 2014

Abstract

We present the influence of Fe-doping (2%, 3% and 4%) on ZnO thin films. For this purpose, structural, electrical and optical proprieties have been investigated by X-ray diffraction, 4-points technique and UV-Visible spectrophotometry. The ZnO:Fe thin films have been deposited by pneumatic spray pyrolysis on glass substrates at different temperatures (350, 400 and 450°C) and fixed molarity (0.1mol/l). The precursor solution is a mixture of zinc acetate dihydrate ($Zn(CH_3COO)_2 \cdot 2H_2O$) and iron chloride hexahydrate ($FeCl_3 \cdot 6H_2O$) dissolved in bi-distilled water. The X-ray diffraction (XRD) analyzes show that all the prepared thin films have a polycrystalline structure dominated by (100), (002) and (101) textured orientations. A resistivity of $2.9 \cdot 10^2 \Omega \cdot cm$ was found for films deposited at 450°C with an iron rate of 3%. The average transmittance was found to be in the range of 45-70% for the different doping rates. The optical band gap energy of the films was found near 3.3 eV.

key words: Thin films, Spray pyrolysis, ZnO:Fe, Resistivity, Band gap energy.

1. Introduction

Zinc oxide (ZnO), a II-VI semiconducting material with a wide direct band gap of 3.3 eV [1], has an advantage of independently controlled charge by changing the doping rate by a transition-metal element (Mn, Co, Fe, etc.) [2-4]. The transition metal-doping in ZnO is very attracting [5] because it leads to new interesting properties [6,7] and is a good candidate method to improve optical properties. In order to use ZnO thin films in an optoelectronic device, the performances of the device have to be adjusted by controlling the optical, structural and electronic properties of the films. Bae et al. [8] reported that ZnO thin films showed different emission bands depending on the doping material.

ZnO:Fe semiconductors have a number of attractive applications, such as: gas sensor devices [9], transparent electrodes [10], piezoelectric devices [11], etc. Several techniques have been used to produce many distinct zinc oxide films: chemical vapor deposition [12], radio frequency magnetron sputtering [13], Sol-Gel [14], spray pyrolysis, etc. [15-18]. In this work, we have investigated the properties of ZnO-doped films deposited by spray pyrolysis. For this purpose, the optical, structural and electrical properties of Fe-doped ZnO were studied when

varying Fe content and substrate temperature. In order to determine the doping effect of the transition metal (²⁷Fe) in ZnO on these properties, we carried out UV-Visible spectro-photometry, DRX analysis and 4-points measurements, respectively.

2. Experimental

A spray pyrolytic technique was used to obtain Fe doped zinc oxide thin films. The experimental set up was previously described [20, 21]. The films were prepared by a solution with fixed concentration (0.1 mol/l) of zinc acetate dihydrate ($Zn(CH_3COO)_2 \cdot 2H_2O$) and iron chloride hexahydrate ($FeCl_3 \cdot 6H_2O$) dissolved in doubly distilled water onto glass substrates. The substrate temperature was varied between 350 and 450°C and measured via a Chromel-Alumel thermocouple. X-ray diffraction was used to determine the crystallographic structure. The size of crystallites were estimated using the Scherrer's formula [22]:

$$D = \frac{0.9 \lambda_X}{\beta \cos \theta} \quad (1)$$

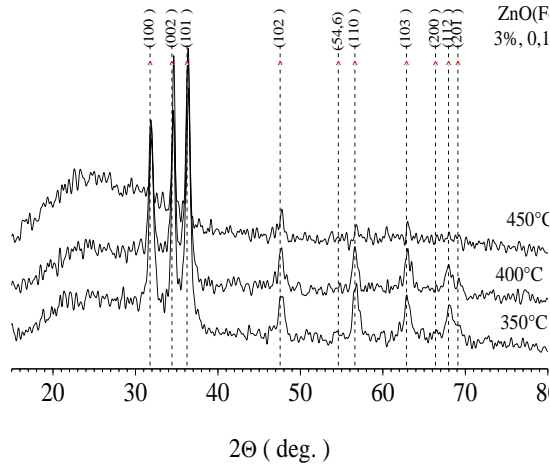


Fig.1. X-ray diffraction patterns of doped ZnO by 3% of iron thin films deposited by spray pyrolysis using different temperatures at 0.1M.

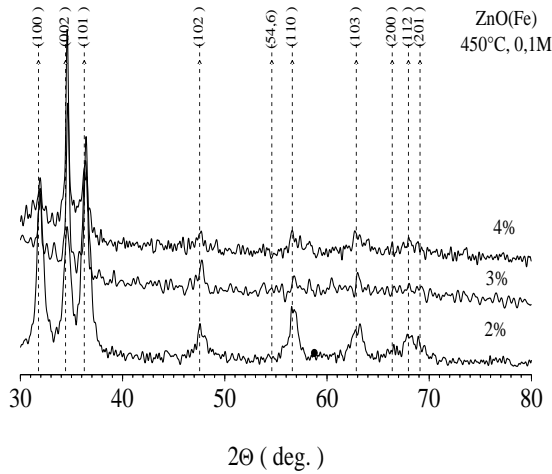


Fig.2. X-ray diffraction patterns of ZnO:Fe thin films deposited by spray pyrolysis using different doping rates at fixed molarity (0.1M) and temperature (450°C).

where λ_x , θ and β are the X-ray wavelength (1.54056 Å), Bragg diffraction angle of XRD peak in degrees, and the full width at half maximum (in radian) of [002], [101], [100] orientations, respectively.

The optical transmission spectra $T(\lambda)$ of the films were obtained using the Shimadzu-3101PC UV-Vis-NIR spectrophotometer. From these spectra the values of the optical energy gap were deduced using formula (2) for direct band gap semiconductors [23]:

$$(\alpha h\nu)^2 = A(h\nu - E_g) \quad (2)$$

where A is a constant. E_g is obtained from $(\alpha h\nu)^2$ vs. $h\nu$ plot when $(\alpha h\nu)^2=0$. The absorption coefficient α

is deduced from $T(\lambda)$ through the Beer-Lambert law [24]:

$$\alpha = \frac{1}{d} \ln \frac{1}{T} \quad (3)$$

where d is the film thickness. Another important parameter that characterizes the disorder in the material is Urbach energy parameter (E_{urb}) determined from Urbach law [25,26]:

$$\ln \alpha = \ln \alpha_0 + \frac{h\nu}{E_{\text{urb}}} \quad (4)$$

The electrical properties of the films were determined using the I-V characteristics measured by the 4-points technique.

3. Results and Discussion

a. Structural Characterization

Typical XRD patterns of ZnO:Fe thin films with various rates of iron doping (2%, 3% and 4%) are presented in figures 1 and 2. In all cases, the observed diffraction peaks are indexed to standard hexagonal wurtzite ZnO structure. No secondary phases or impurity peaks can be identified which demonstrates that the dopant is well integrated into the lattice sites during the synthesis process. A small shift of the peaks to higher angles with the increase of Fe doping compared to those of pure ZnO was observed. The minor peak shift is usually assigned to the successful incorporation of dopant irons in the host matrix [27]. The lattice constants of Fe (3%) doped ZnO ($a=3.2405$ Å, $c=5.2112$ Å) were found to be slightly larger than those of pure ZnO ($a=3.2491$ Å, $c=5.2062$ Å). This observation is similar to the case in transition metal (Mn, Cu and Ni) doped ZnO studied by Ekambaram et al. [28].

The variations of estimated grain size D with temperature and doping rate are represented on figure 3. The size of the grains increases from 100 to 335 Å when the percentage of doping varies from 2 to 4% and the temperature change between 350 to 450°C at fixed concentration. This evolution is normal because the increase in the percentage of doping or treatment is always accompanied by an increase in the size of the grains whatever the technique of development used [29]. The samples deposited at high temperature grow more slowly, which is equivalent to an annealing of the layer in formation, involving an increase in the size of the grains. The results obtained here agree well with the works of Chopra and Roth et al. [30-32] that showed that the grain size increases with the film thickness.

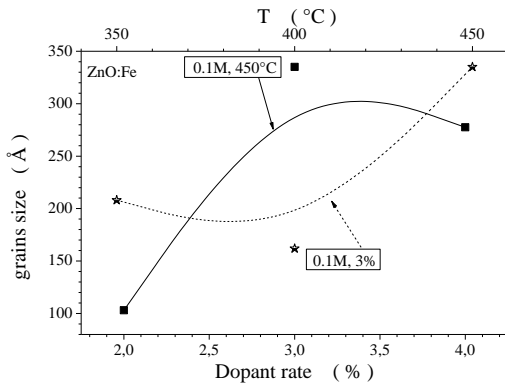


Fig.3. Variation of the estimated grain size with the doping rate and the temperature at 0.1M.

b. Optical Characterization

The transmittance spectra $T(\lambda)$ of ZnO:Fe films deposited on glass are shown on figures 4 and 5. Transmittance strongly depends on the substrate temperature and the doping rate. As mentioned above, at low doping rate (2%), the transmittance of the layers is relatively high for wavelengths higher than 500 nm. However, there are many causes for the transparency of the thin films deposited such as: the wavelength, substrate temperature, concentration of the solution and the reaction of decomposition of the droplets on the substrate. On the other hand, at high temperature, the transmittance is raised and depends slightly on the molarity and the doping rate. This indicates a complete thermal decomposition of the droplets involving the formation of a material close to the stoichiometry, which leads to layers of lower thicknesses. This is in good agreement with the results of Zaouk et al. [33] who showed that at higher temperatures, there is enough energy available for the thermal decomposition, solvent evaporates before the droplets reach the substrate and only the solid precursor reaches the substrate where thermal decomposition occurs. Consequently, the grown material is dense and the obtained films are relatively thin. That is also a consequence of the disappearance of the impurities following volatilization, at high temperature, of the secondary reaction products. The values found for the transmittance are about 45 to 70%, because the doping by iron reduces the transparency of the thin ZnO layers in the visible region.

c. Electrical Characterization

The electrical properties of the ZnO thin layers are of a considerable interest, in particular in the photovoltaic applications. Fig. 6 represents the variation of the electrical conductivity σ of the ZnO:Fe thin films with the doping rate. We can see

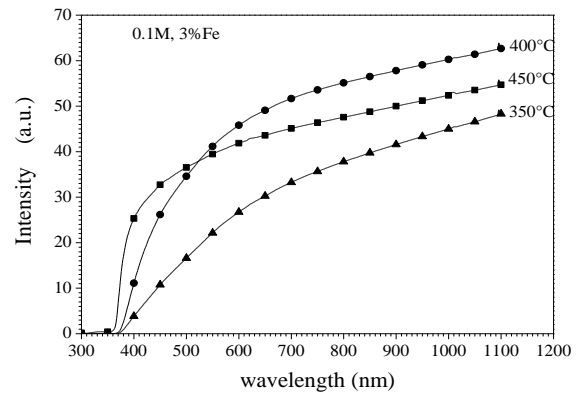


Fig.4. Variation of the optical transmittance with the wavelength for different temperatures of deposition at 0.1M and 3% (Fe)

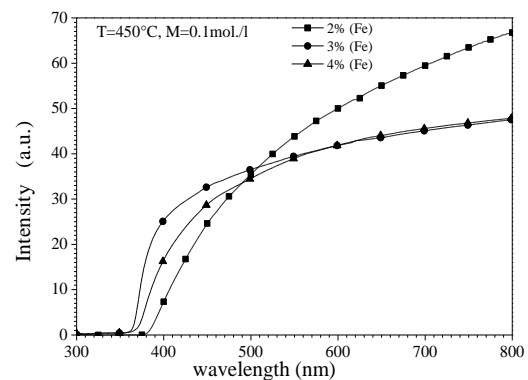


Fig.5. Variation of the optical transmittance with the wavelength for different doping rates at 0.1M and 450°C.

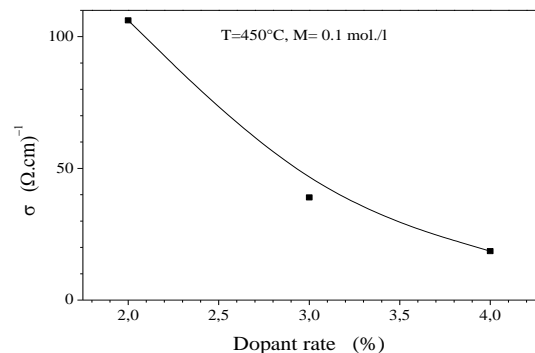


Fig.6. Variations of the electrical conductivity with the doping rate of layers deposited at 450°C.

that the electrical conductivity decreases with the doping rate. Figure 7 shows the variation of σ with the substrate temperatures T , for a fixed concentration and a doping rate (0.1M and 3% respectively). The electrical conductivity increases with substrate temperature. A resistivity of $2.9 \cdot 10^3 \Omega \cdot \text{cm}$ was found for films deposited at 450°C with an iron rate of 3%.

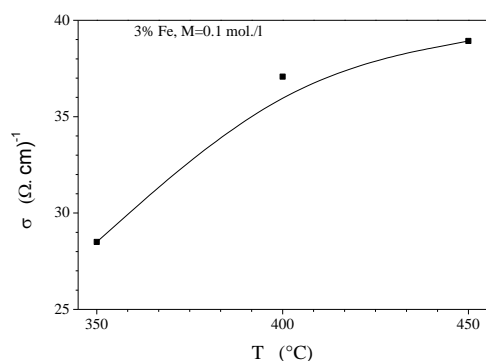


Fig.7. Variations of the electrical conductivity with the temperature of deposition at fixed concentration and doping rate.

4. Conclusion

ZnO:Fe semiconducting metal oxides were successfully synthesized by the spray pyrolysis method. The structural, optical and electrical properties of the Fe-doped ZnO thin films were investigated. The observed diffraction peaks are indexed to standard hexagonal wurtzite ZnO structure. No visible secondary phases for the doped ZnO thin films was found in the XRD patterns and the peaks were shifted to higher angles with the increase of Fe doping rate indicating the incorporation of doping atoms in the host matrix. The values found for the transmittance are about 45 to 70% in the visible. The electrical conductivity increases with substrate temperatures. Moreover, the temperature dependence measurements show that the electrical conductivity is controlled by thermally activated processes.

Reference:

- [1] Seonghoon Baek, Jaemin Song, Sangwoo Lim, "Improvement of the optical properties of ZnO nanorods by Fe doping", *Physica B* 399 (2007) 101-104.
- [2] Z. jin, T. Fukumura, M. Kawasaki, K. Ando, H. Saito, T. Sekiguchi, Y.Z. Yoo, M. Murakami, Y. Matsumoto, T. Hasegawa, H. Koinuma, *Appl. Phys. Lett.* 78 (2001) 3824.
- [3] T. Fukumura, Z. Jin, M. Kawasaki, T. Shono, T. Hasegawa, S. Koshihara, H. Koinuma, *Appl. Phys. Lett.* 78 (2001) 958.
- [4] S.J. Pearton, C.R. Abernathy, M.E. Overberg, G.T. Thaler, D.P. Norton, N. Theodoropoulou, A.F. Hebard, Y.D. Park, F. Ren, J. Kim, L.A. Boatner, *J. Appl. Phys.* 93 (2003) 1.
- [5] T. Dietl, H. Ohno, F. Matsukura, J. Cibert, D. Ferrand, *Science* 287 (2000) 1019.
- [6] X.M. Cheng, C.L. Chien, *J. Appl. Phys.* 93 (2003) 7876.
- [7] K. Ueda, H. Tabata, T. Kawai, *Appl. Phys. Lett.* 79 (2001) 988.

- [8] S.Y. Bae, C.W. Na, J.H. Kang, J. Park, *J. Phys. Chem. B* 109 (2005) 2526.
- [9] C. H. Kwon, H. K. Hong, D. H. Yun, K. Lee, S. T. Kim, Y. H. Roh, B. H. Lee, *Sensors and Actuators B* 24-25 610 (1995).
- [10] S. Major, S. Kumar, M. Bhatnagar and K.L. Chopra, *Appl. Phys. Lett.* 49 394 (1986).
- [11] M.G. Ambia, M.N. Islam, M. Obaidul Hakim, *J. Mater. Sci.* 27 5169 (1992).
- [12] Jianhua Hu and Roy G. Gordon, *J. Appl. Phys.* 71 880 (1992).
- [13] O. Takai, M. Futsuhara, G. Shimizu, C. P. Lungu, J. Nozue, *Thin Solid Films* 31 117 (1998).
- [14] M. Ohyama, H. Kozuka and T. Yoko, *Thin Solid Films* 306 78 (1997).
- [15] J. L. van Heerden and R. Swanepoel, *Thin Solid Films* 299 72 (1997).
- [16] M. Krunk and E. Mellikov, *Thin Solid Films* 270 33 (1995).
- [17] S. Oktik, G.J. Russell and A.W. Brinkman, *J. Cryst. Growth* 159 195 (1996).
- [18] F. Paraguay, W. Estrada L., D. R. Acosta N., E. Andrade, M. Miki-Yoshida, *Thin Solid Films* 350 192 (1999).
- [19] M. Miki-Yoshida and E. Andrade, *Thin Solid Films* 224, 87 (1993).
- [20] Herissi Labidi, Mémoire de magister soutenu le 09/03/2008, Université Larbi Ben M'Hidi - Oum El Bouaghi, Algérie.
- [21] Lazhar Hadjeris, Labidi Herissi, M Badreddine Assouar, Thomas Easwarakhanthan, Jamal Bougdira, Nadhir Attaf and M Salah Aida, *Semicond. Sci. Technol.* 24 035006 (6pp), 2009.
- [22] G. Fang, D. Li, B. Yao, *Vacuum*, 68 (2003) 363
- [23] J. Tauc, A. Menthe, *J. Non-Cryst. Sol.* 8-10 (1972) 569-585.
- [24] S. ROY and S. BASU, *Bull. Mater. Sci.* 25 (2002) 513-515.
- [25] F. Urbach, *Phys. Rev.* 92 (1953) 1324-1324.
- [26] A. Bougrine, A. El Hichou, M. Addou, J. Ebothé, A. Kachouna and M. Troyon, *Mater. Chem. Phys.* 80 (2003) 438-445.
- [27] Panigrahy B, Aslam M and Bahadur D 2010 *J. Phys. Chem. C* 114 11758-63
- [28] S Ekambaram, Y Iikubo and A Kudo *J. Alloys Compd.* 433 237(2006)
- [29] A. Moustaghfir, Thèse de doctorat, Université Blaise Pascal, D.U. 1540 (2004).
- [30] M.T. Mohammad, A.A. Hashim and M.H. Al-Maamory, *Materials Chemistry and Physics* 99 (2006) 382-387.
- [31] K.L. Chopra, S. Major, *Thin Solid Films* 102 (1983).
- [32] O.P. Rath, D.F. William, *J. Appl. Phys.* 52 (1981) 11.
- [33] D. Zaouk, Y. Zaatat, R. Asmar, J. Jabbour, *Microelectronics Journal* 37 (2006) 1276-1279.